

Structure and assembly of the dystrophin glycoprotein complex

<https://doi.org/10.1038/s41586-024-08310-2>

Received: 13 June 2024

Accepted: 30 October 2024

Published online: 11 December 2024

 Check for updates

Li Wan^{1,2,3,10}, Xiaofei Ge^{4,10}, Qikui Xu^{1,2,3,10}, Gaoxingyu Huang^{1,2,3,10}, Tiandi Yang^{5,6,7,8,9}, Kevin P. Campbell^{5,6,7,8}, Zhen Yan^{1,2,3}✉ & Jianping Wu^{1,2,3}✉

The dystrophin glycoprotein complex (DGC) has a crucial role in maintaining cell membrane stability and integrity by connecting the intracellular cytoskeleton with the surrounding extracellular matrix^{1–3}. Dysfunction of dystrophin and its associated proteins results in muscular dystrophy, a disorder characterized by progressive muscle weakness and degeneration^{4,5}. Despite the important roles of the DGC in physiology and pathology, its structural details remain largely unknown, hindering a comprehensive understanding of its assembly and function. Here we isolated the native DGC from mouse skeletal muscle and obtained its high-resolution structure. Our findings unveil a markedly divergent structure from the previous model of DGC assembly. Specifically, on the extracellular side, β -, γ - and δ -sarcoglycans co-fold to form a specialized, extracellular tower-like structure, which has a central role in complex assembly by providing binding sites for α -sarcoglycan and dystroglycan. In the transmembrane region, sarcoglycans and sarcospan flank and stabilize the single transmembrane helix of dystroglycan, rather than forming a subcomplex as previously proposed^{6–8}. On the intracellular side, sarcoglycans and dystroglycan engage in assembly with the dystrophin–dystrobrevin subcomplex through extensive interaction with the ZZ domain of dystrophin. Collectively, these findings enhance our understanding of the structural linkage across the cell membrane and provide a foundation for the molecular interpretation of many muscular dystrophy-related mutations.

Skeletal and cardiac muscle fibres undergo continuous deformation and shortening during contraction, which necessitates a mechanism for force transmission to maintain the structural integrity of the muscle cell membrane, known as the sarcolemma^{9,10}. The DGC is a multimeric complex that safeguards the sarcolemma against mechanical stress and mitigates contraction-induced injury by establishing a robust mechanical scaffold that links the extracellular matrix (ECM) to the intracellular actin cytoskeleton^{1–3,7}. Besides its primary functions in muscle tissues, the DGC also provides structural support for neuronal membranes and to regulate neurotransmitter signals at the neuromuscular junction^{11,12}. Additionally, the DGC acts as a pivotal nexus for cell signalling, serving as a docking site for various intracellular signalling proteins¹³. Thus the DGC is actively involved in regulating cell mechanotransduction, survival, migration and growth.

The composition of the DGC varies slightly across different tissues and is generally considered to consist of three parts: the cytosolic dystrophin subcomplex, the dystroglycan subcomplex and the sarcoglycan–sarcospan subcomplex^{6,8} (Extended Data Fig. 1a). Dystrophin was initially isolated from rabbit skeletal muscle and was

the first DGC component to be identified^{1,14}. It is a large filamentous rod protein (more than 3,600 amino acids) that possesses multiple domains, including a cluster of 24 spectrin domains flanked by the N-terminal and C-terminal domains, enabling it to serve as a platform that interacts with many other proteins, which are collectively known as dystrophin-associated proteins^{8,15} (DAPs). Notably, the N terminus of dystrophin contains an actin-binding domain that binds to F-actin, thereby establishing a physical connection between the DGC and the actin-based cytoskeleton¹⁶. The dystrophin subcomplex also include intracellular DAPs such as dystrobrevin and syntrophins. Dystrobrevin shares sequence homology with the C-terminal region of dystrophin, and syntrophins serve as adapter proteins to facilitate the association between dystrophin and various signalling proteins, such as neuronal nitric oxide synthase (nNOS) and caveolin-3^{7,17}.

The dystroglycan subcomplex consists of a heterodimer of α -dystroglycan (α -DG) and β -dystroglycan (β -DG), which are derived from the same precursor protein—dystroglycan^{18,19}. The dystroglycan protein is encoded by *DAG1*, and is processed by post-translational cleavage to produce α -DG and β -DG. α -DG resembles a dumbbell, consisting

¹Key Laboratory of Structural Biology of Zhejiang Province, School of Life Sciences, Westlake University, Hangzhou, China. ²Westlake Laboratory of Life Sciences and Biomedicine, Hangzhou, China. ³Institute of Biology, Westlake Institute for Advanced Study, Hangzhou, China. ⁴State Key Laboratory of Membrane Biology, Beijing Frontier Research Center for Biological Structure, School of Life Sciences, Tsinghua University, Beijing, China. ⁵Howard Hughes Medical Institute, University of Iowa Roy J. and Lucille A. Carver College of Medicine, Iowa City, IA, USA. ⁶Senator Paul D. Wellstone Muscular Dystrophy Specialized Research Center, University of Iowa Roy J. and Lucille A. Carver College of Medicine, Iowa City, IA, USA. ⁷Department of Molecular Physiology and Biophysics, University of Iowa Roy J. and Lucille A. Carver College of Medicine, Iowa City, IA, USA. ⁸Department of Neurology, University of Iowa Roy J. and Lucille A. Carver College of Medicine, Iowa City, IA, USA. ⁹Department of Immunology, Harvard Medical School, Boston, MA, USA. ¹⁰These authors contributed equally: Li Wan, Xiaofei Ge, Qikui Xu, Gaoxingyu Huang. ✉e-mail: yanzhen@westlake.edu.cn; wujianping@westlake.edu.cn

of two extracellular globular domains linked by a flexible region known as the mucin-like domain. The mucin-like domain is heavily glycosylated and mediates the binding of ECM proteins through its glycans²⁰. β -DG contains a single transmembrane helix; its N-terminal extracellular domain interacts with the C-terminal region of α -DG, whereas its C-terminal cytoplasmic region associates with several intracellular components of the DGC, linking the ECM to the cytoskeleton²¹. The sarcoglycan–sarcospan subcomplex in skeletal muscle comprises α -, β -, γ - and δ -sarcoglycans and sarcospan. Additionally, ϵ - and ζ -sarcoglycans have been identified as capable of replacing α - and γ -sarcoglycans in other tissues, respectively⁸. All sarcoglycans contain a single transmembrane helix and an extracellular domain, whereas sarcospan has four transmembrane helices and belongs to the tetraspanin family^{8,22}.

The physiological and pathological importance of the DGC is underscored by its strong association with muscular dystrophies, a spectrum of disorders characterized by muscle weakening and degeneration⁴. Mutations in the DGC components have been identified as primary causes of multiple types of muscular dystrophies in humans^{4,8}. Specifically, mutations in the dystrophin gene result in dystrophinopathies, including Duchenne muscular dystrophy (DMD) and Becker muscular dystrophy^{5,23}. DMD is one of the most common and severe types of muscular dystrophy, typically presenting in early childhood and rapidly progressing. It affects about 1 in every 3,500 to 5,000 males worldwide and currently lacks a cure^{5,24}. Additionally, loss-of-function mutations in sarcoglycan genes result in sarcoglycanopathies, which are subtypes of limb girdle muscular dystrophy²⁵ (LGMD). Abnormalities in the post-translational processing of dystroglycan alter the glycosylation of α -DG and disrupt its interactions with the ECM, which are associated with various forms of LGMD and congenital muscular dystrophy^{25–28}. Moreover, owing to the multifaceted function of the DGC, aberrations that disrupt its structure and function also contribute to the development of other serious diseases in the heart and brain, including dilated cardiomyopathy, cognitive impairment and neuronal migration disorders^{12,29,30}. Consequently, the DGC possesses substantial physiological and clinical importance as a promising therapeutic target for the treatment of diverse muscular dystrophies and other related disorders³¹.

Over the past three decades, extensive genetic and biochemical investigations have provided valuable insights into the compositions and functions of the DGC¹⁷. The structures of some soluble domains of DGC components have been characterized, including the actin-binding domain³², the first spectrin domain³³, and the C-terminal WW domain-containing region of dystrophin³⁴, as well as the N-terminal domain of α -DG³⁵. However, our understanding of how the DGC is assembled and the molecular mechanisms by which it functions is limited by the lack of high-resolution structural information of the intact complex. The prevailing model of DGC assembly, primarily derived from biochemical studies, posits that the dystroglycan subcomplex is in the centre of DGC and is pivotal for interactions with cytoplasmic dystrophin, and that the sarcoglycan–sarcospan subcomplex is positioned at the periphery^{6,7} (Extended Data Fig. 1a).

In this study, we isolated the native DGC from mouse skeletal muscle and used single-particle cryo-electron microscopy (cryo-EM) to determine its structure. Our study provides insights into the assembly mechanism of the DGC. The cryo-EM structure diverges from the previous model, revealing that sarcoglycans and sarcospan flank the two sides of the transmembrane helix of β -DG, and that sarcoglycans bind directly to dystrophin. This structure serves as an important foundation for the mechanistic interpretation of many muscular dystrophy-related mutations that have been identified in clinical research over the past few decades.

Isolation of the native DGC sample

Laminin- α 2 in the ECM was previously reported to interact with the glycans on α -DG through the laminin G-like (LG) domains 4 and 5

(LG4 and LG5) in a Ca^{2+} -dependent manner³⁶. We recombinantly expressed the Flag-tagged LG4 and LG5 domains of laminin- α 2 and used it as an affinity bait to isolate the endogenous DGC from mouse skeletal muscle tissue (Extended Data Fig. 1b,c). Gel filtration of the purified sample showed a small peak at a molecular weight larger than the 669 kDa molecular marker, which is reasonable for the size of intact DGC (Extended Data Fig. 1d). Western blotting of the peak fractions showed co-migration of multiple detected DGC components, suggesting that they remain as an intact complex during purification (Extended Data Fig. 1e and Supplementary Fig. 1a). Mass spectrometry analysis of the peak fractions verified the presence of all previously known components of the DGC, confirming that we were successful in isolating the native complex (Extended Data Fig. 1f).

Determination of the mouse DGC structure

Using the native DGC sample, we subsequently made grids for cryo-EM structure determination. After data processing, we generated a reconstruction map (Map 1) at an overall resolution of 3.2 Å (Extended Data Fig. 2). However, density at the intracellular region of Map 1 was relatively weak, indicating inherent conformational flexibility in this region. To further improve the resolution of the intracellular domains, we performed additional 3D classifications with a mask focused on the intracellular region. This yielded a reconstruction map (Map 2) at an overall resolution of 3.5 Å with much improved intracellular density that enabled local composition assignment and structural analysis (Extended Data Figs. 2 and 3). Guided by the two maps, we were able to build a final DGC model comprising nine components, including α -, β -, γ - and δ -sarcoglycans, α -DG, β -DG, sarcospan, dystrophin and dystrobrevin (Fig. 1 and Extended Data Tables 1 and 2). We also identified multiple glycosylation modification sites and disulfide bonds on some components (Extended Data Table 2). In addition, we identified several lipid molecules that resemble phosphatidylserine and cholesterol in the structure, which are likely to contribute to the assembly of the complex (Fig. 1). Although the LG4 and LG5 domains of laminin- α 2 was used to isolate the DGC, we did not observe these domains and their interacting glycans on α -DG in the structure, probably owing to the disordered nature of the mucin-like domain of α -DG. The final overall resolved structure displayed a pronounced elongation in height, with dimensions of approximately 90 Å × 100 Å × 250 Å (Fig. 1). The overall elongated structure of the DGC facilitates effective contact with ECM proteins and intracellular-associated proteins, thereby fulfilling its role in connecting the two sides of the cell membrane. Deviating from the previous DGC model (Extended Data Fig. 1a), the structure reveals that sarcoglycans are central in mediating complex assembly by forming a characteristic tower-like extracellular domain (hereafter referred to as the ECD tower). Additionally, rather than forming a subcomplex together, sarcoglycans and sarcospan are spatially separated, with the transmembrane helix of β -DG positioned between them (Fig. 1).

Structure of the ECD tower

The elongated ECD tower of the DGC is formed by co-assembly of β -, γ - and δ -sarcoglycans (Fig. 2a). The three sarcoglycans are homologous and share a similar overall topology, with a single N-terminal transmembrane helix followed by 26 β -strands in β -sarcoglycan and 27 β -strands in γ - and δ -sarcoglycans (Extended Data Fig. 4a,b). The transmembrane helices of the three sarcoglycans form a stable helical bundle, primarily mediated by hydrophobic interactions (Fig. 2a,b). In addition, each of the three components includes a conserved asparagine that mediates specific interactions of the helical bundle (Fig. 2a). The extracellular β -strands of the 3 components co-fold with each other to form a rigid β -helix with a height of approximately 135 Å. The β -helix is assembled in the manner of staggered, right-handed rising spiral, with three faces designated as (a)–(c) (Fig. 2a and Extended Data Fig. 4a). Within each

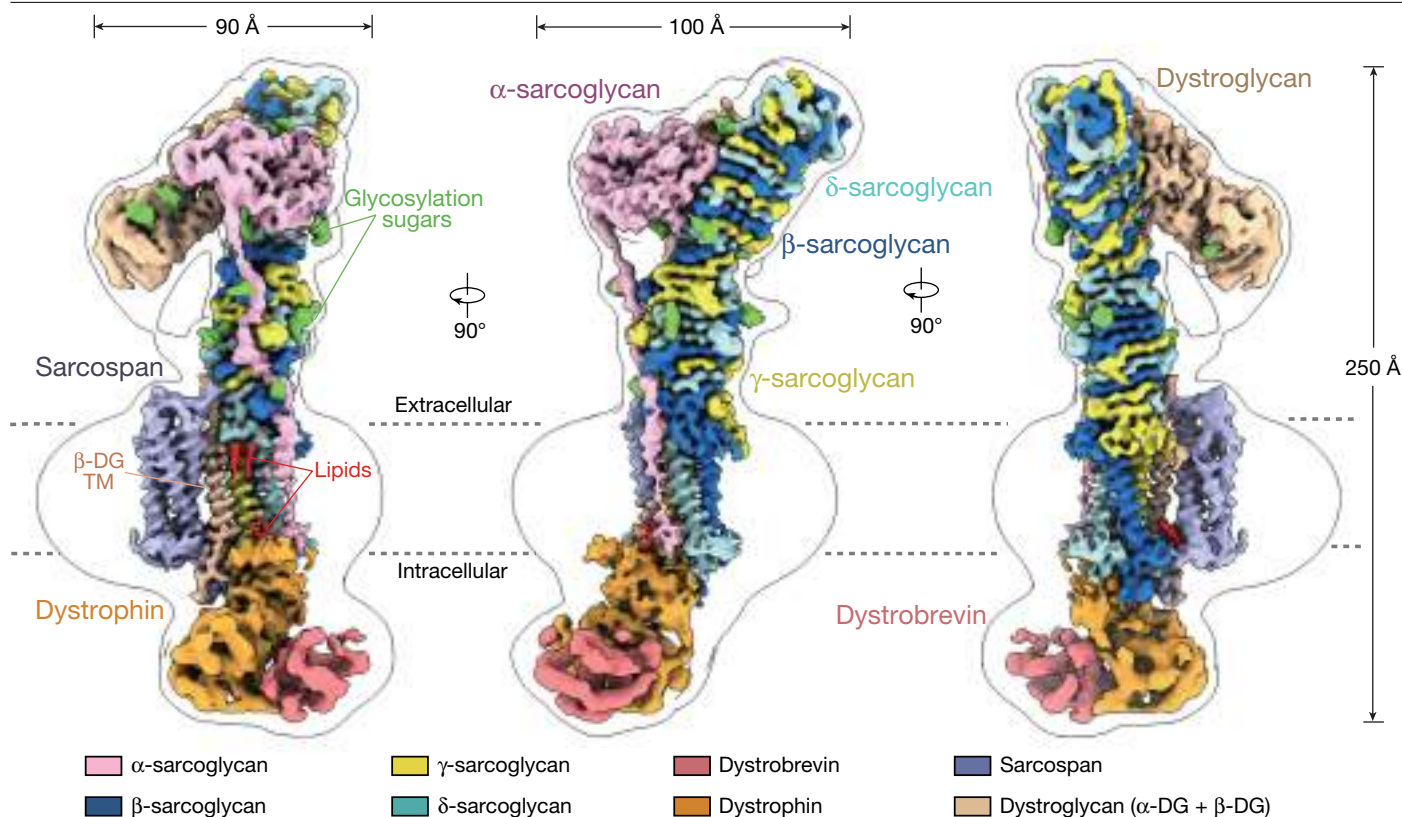


Fig. 1 | Cryo-EM reconstruction of the DGC from mouse skeletal muscle. The overall cryo-EM map of the DGC coloured by subunit and shown in three side views (Electron Microscopy Data Bank (EMDB): EMD-39568, contour level: 0.41). A map low-pass filtered to 16 Å (contour level: 0.09) is shown in transparency to indicate the transmembrane region surrounded by the

detergent micelle densities. The flexible linker of dystroglycan between the extracellular domain and the transmembrane helix is weak and can be observed in the low-pass filtered map. The measures of the three dimensions are based on the coloured map. TM, transmembrane helix.

face of the ECD tower, β-strands from the three sarcoglycans alternate and run parallel to each other, with few exceptions. For example, β3–β4 and β9–β11 of all three sarcoglycans, β12–β13 of β-sarcoglycan and β12–β14 of γ- and δ-sarcoglycans form anti-parallel β-strands within the same face of the ECD tower, respectively (Extended Data Fig. 4a).

The exterior surface of the ECD tower is highly hydrophilic with many charged patches, which enables it to serve as docking sites for other components (Fig. 2b). The distal tip of the ECD tower is stabilized by six pairs of conserved disulfide bonds, with each component contributing two pairs (Fig. 2c and Extended Data Table 2). Specific interactions among Lys288 of β-sarcoglycan, Glu263 of γ-sarcoglycan and E261 of δ-sarcoglycan fully seal the distal tip (Fig. 2c). A cross-sectional view of the main body of the ECD tower shows a triangle shape, featuring many hydrophobic residues buried in the interior of the ECD tower (Fig. 2d). There are five N-linked glycosylation sites in the ECD tower, including Asn160, Asn213 and Asn260, which are specific to β-sarcoglycan, and a conserved site between Asn110 of γ-sarcoglycan and Asn108 of δ-sarcoglycan (Fig. 2a,d and Extended Data Fig. 4b).

Notably, the ECD tower is bent in the middle, forming a distinctive angle of around 140° (Fig. 2a,b). Structural analysis of the bending site reveals that β14 of β-sarcoglycan deviates by approximately 70° from β12–β13 of face (a) to face (b), rather than forming a locally anti-parallel β sheet with β12–β13, a feature observed in γ- and δ-sarcoglycans. As a result, β15 of β-sarcoglycan transitions directly to face (c), instead of pairing with β14 of γ-sarcoglycan in face (b) as expected (Fig. 2e). Sequence alignment among β-, γ- and δ-sarcoglycans indicates a relatively lower sequence homology of β-sarcoglycan compared with the other two sarcoglycans, and the sequence near β14 of β-sarcoglycan is even less conserved compared with the other regions (Extended Data Fig. 4b). Thus, the sequence and structural divergence of β-sarcoglycan

in this region contributes to the characteristic bending of the ECD tower. This structural feature of the ECD tower is likely to facilitate its capacity to accommodate the simultaneous binding of α-sarcoglycan and dystroglycan, as described below. Moreover, we speculate that the bending of the ECD tower also enables it to transmit force in various directions, which aligns with the functional role of the DGC in transmitting both longitudinal and lateral forces during muscle contraction^{9,37}.

Two domains attach to the ECD tower

The extracellular domains of dystroglycan (492–712) and α-sarcoglycan (24–253) were found to attach to the ECD tower (Fig. 3a). Notably, these two domains share a similar overall fold, despite having relatively low sequence identity (less than 20%). Both domains contain an immunoglobulin-like domain and a peptidase S72 domain (P domain) (Fig. 3a and Extended Data Fig. 5a). We identified multiple N-linked glycosylation modifications in the P domains of both components (Fig. 3a and Extended Data Table 2). Notably, the previously reported post-translational cleavage site on dystroglycan, which generates α-DG and β-DG, is located within the P domain¹⁸ (corresponding to G651–S652 in mouse) (Fig. 3a and Extended Data Fig. 5a). Therefore, the resolved immunoglobulin-like domain of dystroglycan belongs to α-DG and the P domain is shared by both α-DG and β-DG. This structural observation may explain the strong interaction between α-DG and β-DG even after proteolysis, as previously reported^{21,28}.

The N-terminal domain of α-DG (28–312) was not observed in the structure, owing to post-translational removal³⁸. The subsequent mucin-like domain (313–483), predicted to be disordered, was also unresolved. The crystal structure of N-terminal domain of α-DG has been reported previously, and includes an immunoglobulin-like

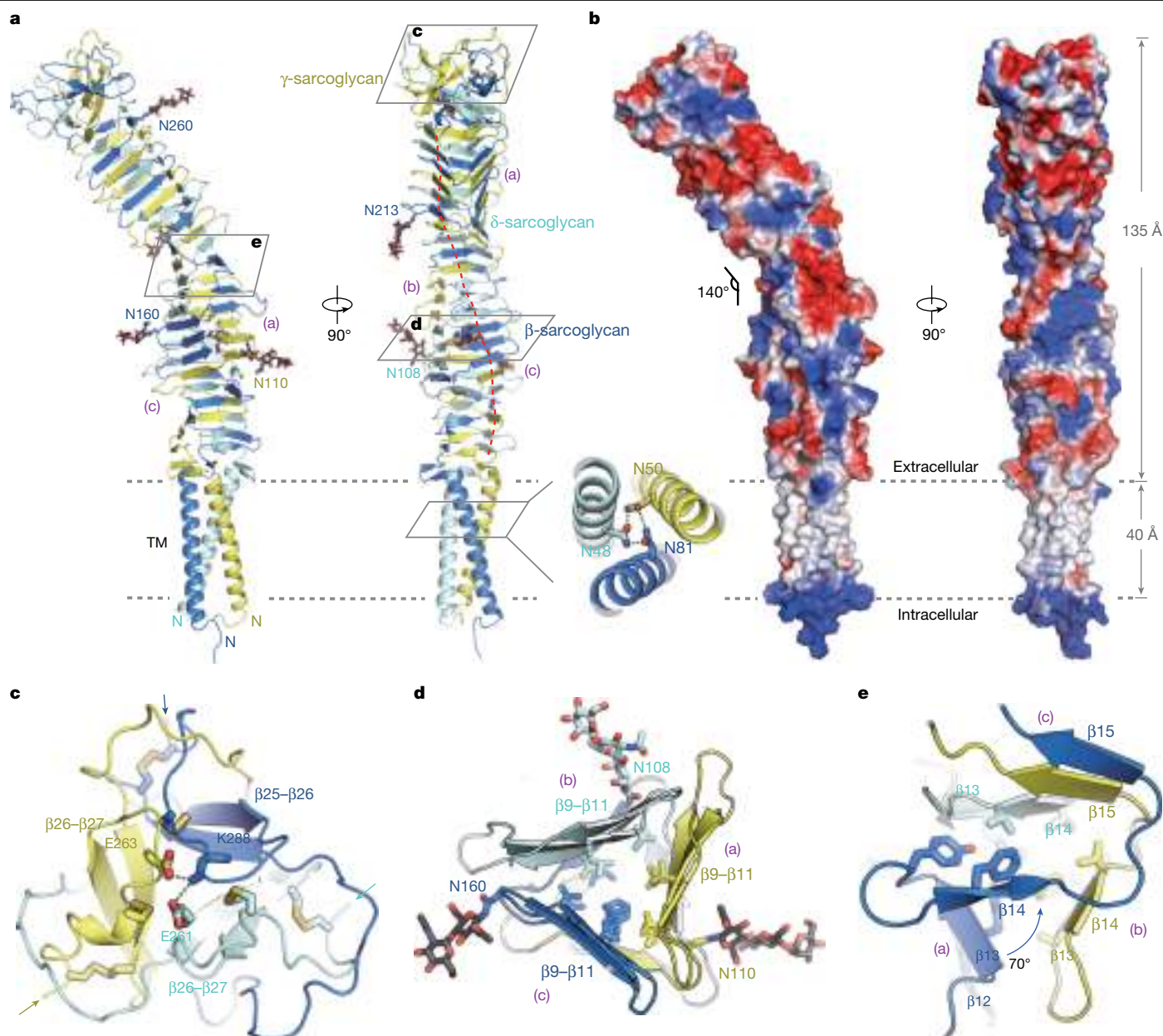


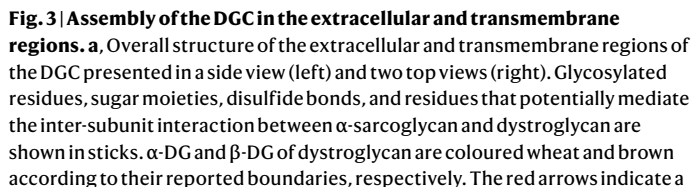
Fig. 2 | Structure of the ECD tower. **a**, Overall structure of the ECD tower shown in two side views. The sugar moieties in the glycosylation sites are shown as sticks. The three faces of the ECD tower are labelled as (a)–(c). Face (c) of the ECD tower is indicated by a red dashed line. Bottom right, close-up view of the transmembrane region observed from the extracellular side. **b**, Electrostatic surface of the ECD tower shown in the same views as in **a**. Red indicates negatively charged regions and blue indicates positively charged regions.

c, Close-up view of the ECD tower tip, as indicated in **a**. The disulfide bonds and residues that mediated inter-subunit interactions are shown as sticks. Hydrogen bonds are presented by dashed lines. The C terminus of each component is indicated by an arrow. **d**, **e**, Enlarged views of the corresponding regions indicated in **a**. The residues that face the interior of the ECD tower and the sugars are shown as sticks.

domain and a P domain³⁵ (Extended Data Fig. 5b). By comparing the crystal structure of the N-terminal domain of α -DG and the resolved extracellular domains of dystroglycan and α -sarcoglycan in our model, we found the relative conformational changes between their immunoglobulin-like domains and P domains (Extended Data Fig. 5b). When superimposing the three structures over their P domains, we observed a subtle conformational variation between the two immunoglobulin-like domains of α -DG, whereas the immunoglobulin-like domain of α -sarcoglycan displays pronounced conformational rotations compared with the two immunoglobulin-like domains of α -DG (Extended Data Fig. 5c).

The resolved immunoglobulin-like domains of α -DG and α -sarcoglycan form specific interactions with the ECD tower; however,

their modes of interaction differ (Fig. 3b). The immunoglobulin-like domain of α -sarcoglycan (24–124) forms multiple hydrogen bonds with face (b) of the ECD tower, primarily involving residues from the β 3– β 4 and β 6– β 7 loops. By contrast, the immunoglobulin-like domain of α -DG (492–594) specifically attaches to the edge of the ECD tower between face (a) and face (b). This attachment mainly involves residues from the β 6 and β 7 strands, rather than the loops of the immunoglobulin-like domain. Moreover, a cation, most probably calcium, is surrounded by several negatively charged residues from both the immunoglobulin-like domain of α -DG and the ECD tower, further stabilizing their specific interactions (Fig. 3b). Notably, the two extracellular domains also interact with each other. The immunoglobulin-like domain of α -DG forms hydrogen bonds with the P domain of α -sarcoglycan. The glycans



The cryo-EM map (Map 2) enabled unambiguous assignment of the C-terminal cysteine-rich (CR) domain of dystrophin, which encompasses a WW domain, two EF-hand domains and a ZZ domain (Fig. 4a and Extended Data Fig. 6a,b). The N-terminal actin-binding domain,

Our structure instead reveals a previously uncharacterized major interaction interface between dystrophin and the transmembrane DAPs through the ZZ domain of dystrophin (Fig. 4a). The ZZ domain of dystrophin is a small cysteine-rich zinc-containing domain, consisting of two α -helices and five β -strands (Fig. 4b,c). The $\alpha 2$ -helix (3358–3374) of the ZZ domain is amphipathic, enabling dystrophin to stably attach to the inner leaflet of the membrane (Fig. 4b). The ZZ domain forms extensive interactions with multiple DGC components near the membrane, including β -sarcoglycan, γ -sarcoglycan and β -DG (Fig. 4a,d). Notably, the residues in the ZZ domain of dystrophin that

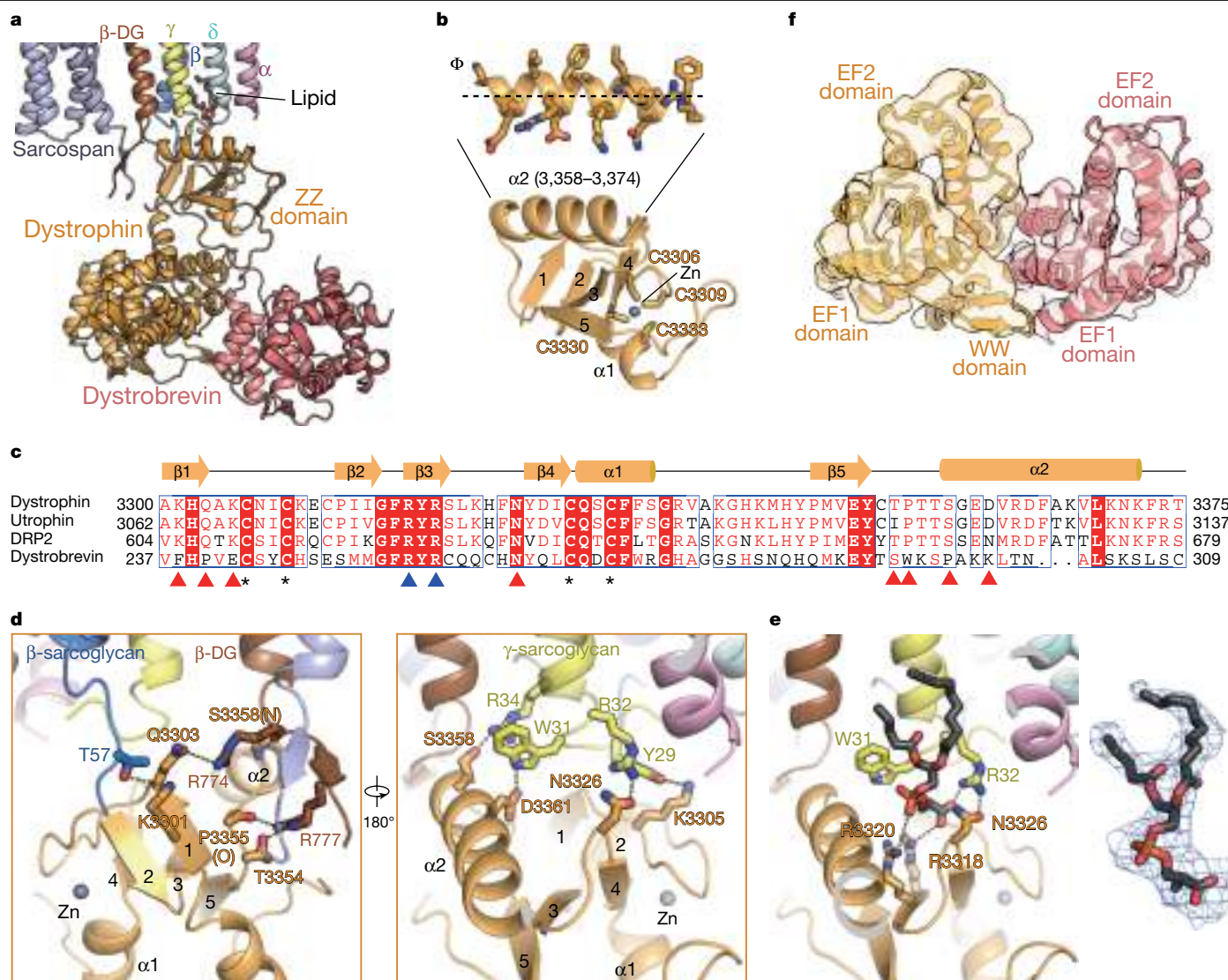


Fig. 4 | Interactions between dystrophin and DAPs. **a**, Overall structure of dystrophin and its nearby subunits. A phosphatidylserine-like lipid is presented in stick view. **b**, Close-up view of the ZZ domain of dystrophin with the amphipathic $\alpha 2$ -helix highlighted. The zinc ion and cysteine residues in the zinc-binding site are shown in sphere and sticks, respectively. **c**, Sequence alignment among the ZZ domains of dystrophin homologues and dystrobrevin. Secondary structure elements are indicated above the sequence. Dystrophin residues that mediate interactions with transmembrane DAPs and lipid binding are indicated by red and blue triangles, respectively. The cysteine residues in

the zinc-binding site are indicated by asterisks. The UniProt IDs for each sequence are as follows: dystrophin, P11531; utrophin, E9Q6R7; DRP2, Q05AA6; dystrobrevin, Q9D2N4. **d**, Specific interactions between the ZZ domain of dystrophin and the transmembrane DAPs. **e**, A phosphatidylserine-like lipid facilitates the inter-subunit interactions between dystrophin and the transmembrane DAPs. The density map of the lipid is shown in blue mesh. **f**, Interaction between dystrophin and dystrobrevin shown in the bottom view. The cryo-EM maps of each component are presented as transparent surfaces.

mediate the specific interactions with other components are highly conserved across dystrophin homologues, but not in the ZZ domain of dystrobrevin (Fig. 4c). This suggests that dystrobrevin, although it also contains a ZZ domain, is unable to compete with dystrophin for association with the transmembrane DAPs. Furthermore, we observed a phosphatidylserine-like lipid molecule bound in the interface between the ZZ domain and γ -sarcoglycan (Fig. 4e). This lipid forms direct interactions with several arginine residues from both γ -sarcoglycan and dystrophin, further stabilizing the association of dystrophin with the transmembrane DAPs.

Dystrophin–dystrobrevin interactions

After the assignment of dystrophin in the cytoplasmic region, an additional globular density near the EF-hand domains of dystrophin

remained unassigned (Fig. 4f). The density of this region was in moderate resolution and did not allow reliable side-chain assignment. We carefully analysed the predicted structures of all potential intracellular DGC components, including dystrophin, dystrobrevin, syntrophins, nNOS and caveolin-3, and found that only the EF-hand domains of dystrobrevin and dystrophin could be well fitted into this density (Fig. 4f and Extended Data Fig. 6a,e). However, this density is unlikely to represent another copy of dystrophin, as dystrophin has been reported to exist as a monomer⁴⁰. We therefore tentatively assigned this density as the EF-hand domains of dystrobrevin (Fig. 4f). It has been reported that dystrobrevin and dystrophin interact through their C-terminal coiled-coil motifs following the ZZ domains⁴¹. Although this interface is supported by the structure predicted by AlphaFold3, it was not resolved in our cryo-EM structure, probably owing to the presence of a flexible linker between the coiled-coil motif and the ZZ domain in both proteins

(Extended Data Fig. 6f). Instead, our structure reveals an additional interaction interface between the EF1 domain of dystrobrevin and the EF2 and WW domains of dystrophin, which has not been previously reported and is supported by the predicted structure (Fig. 4f and Extended Data Fig. 6f). To further verify this previously uncharacterized interface, we conducted a gel filtration binding assay using recombinantly expressed EF-hand domains of the two proteins (Extended Data Fig. 6g and Supplementary Fig. 1b). The results showed that the GST-tagged dystrophin, but not GST alone, co-migrates with dystrobrevin on gel filtration. This indicates a direct interaction between the EF-hand domains of the two proteins, supporting the structural observation. Therefore, our structure, combined with previous data, provides a more comprehensive understanding of the interaction between dystrophin and dystrobrevin.

Mapping of disease-related mutations

Mutations in DGC components are frequently found to be responsible for muscular dystrophies in human patients. Our structure provides a valuable framework for mechanistic interpretations underlying these mutations. We have summarized the pathogenic mutation sites reported to date that could be observed in our structure (Fig. 5a,b and Extended Data Table 3). These mutation sites are found in both the extracellular and intracellular regions of the DGC, in line with its functional role as a linker between the ECM and the intracellular cytoskeleton. Specifically, the ECD tower, the extracellular domain of α -sarcoglycan and the region near the ZZ domain of dystrophin are mutation hotspots (Fig. 5a).

Detailed structural analysis reveals that the disease-related mutations have the potential to disrupt crucial interactions necessary for maintaining complex assembly, resulting in muscular dystrophy. Nonsense mutations, which lead to premature termination of protein translation of one component, are likely to disrupt normal assembly of the entire complex. In particular, nonsense mutations occurring in β -, γ - and δ -sarcoglycans typically lead to severe LGMD or DMD-like phenotypes, probably owing to the improper assembly of the ECD tower (Extended Data Table 3). Missense mutations may cause complex abnormalities by affecting local interactions and domain folding. For instance, R34 and R81 of α -sarcoglycan mediate inter-domain interactions between the immunoglobulin-like domain and the P domain through the formation of multiple hydrogen bonds and salt bridges with nearby residues (Fig. 5c). Mutations at these two sites (for example, R34C, R34H or R81C), as well as at G91 (for example, G91S or G91R) in the middle of the inter-domain interface, are likely to affect the folding and stability of α -sarcoglycan (Fig. 5c and Extended Data Table 3). Notably, severe phenotypes of LGMD have been reported in association with the mutations R34C and R34H (Extended Data Table 3). Consistent with our structural analysis, *in vitro* recombinant expression of the extracellular domain of α -sarcoglycan showed significantly lower expression levels for all 19 tested disease-related mutations compared with the wild type, especially in the fractions corresponding to the monomeric peak (Extended Data Fig. 7a,b and Supplementary Fig. 1c).

Furthermore, the interior core of the ECD tower is buried, with many hydrophobic residues. Mutating these hydrophobic residues to positively charged residues, such as L108R and M100K on β -sarcoglycan (corresponding to L110 and M102 in mouse, respectively), would result in unfavourable local interactions, thereby disrupting the proper folding of the ECD tower. Similarly, the mutation S114F (corresponding to S116 in mouse) on β -sarcoglycan potentially causes a steric clash with nearby phenylalanine, thus affecting the normal assembly of the ECD tower (Fig. 5d). Supporting these analyses, all three mutations lead to severe types of muscular dystrophy in human patients (Extended Data Table 3).

In addition, several cysteine residues have important structural roles, and mutations on them are also likely to affect domain stability.

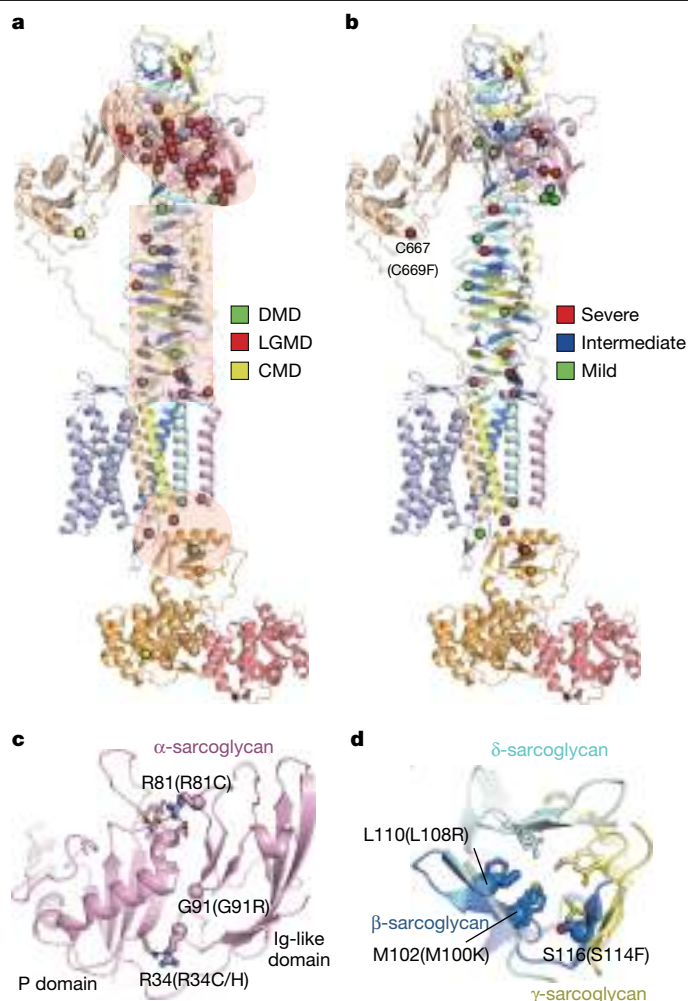


Fig. 5 | Structural mapping of muscular dystrophy-related mutations.

a, Mapping of disease-related mutations on the DGC by muscular dystrophy subtypes. The backbone carbon atoms at disease-related mutation sites are shown as spheres. Three hotspot regions of mutations are shaded. Refer to Extended Data Table 3 for more details. CMD, congenital muscular dystrophy. **b**, Mapping of disease-related mutations by phenotypic severity based on literature reports. Pathogenic mutation sites lacking clearly reported phenotypic severity are coloured grey, and their backbone carbon atoms are not shown. **c**, Examples of mutations that affect the inter-domain interactions within α -sarcoglycan. **d**, Examples of mutations that affect the stability of the ECD tower assembly. The backbone carbon atoms and the side chains of the disease-related mutation sites are shown as spheres and sticks, respectively. The residues that potentially interact with the mutation sites are shown as lines. The corresponding mutations identified in human patients are labelled in parentheses in **c,d**.

For instance, the mutation C283Y in γ -sarcoglycan and the mutation C669F (corresponding to C667 in mouse) in β -dystroglycan would both disrupt a domain-stabilizing disulfide bond within the corresponding subunit (Extended Data Table 2). These two mutations are associated with severe phenotypes of LGMD and muscle-eye-brain disease, respectively (Extended Data Table 3). Notably, whereas the wild-type extracellular domain of dystroglycan showed a high expression level in the HEK293 expression system and exhibited good solution behaviour, a single mutation of Cys667 to phenylalanine completely abolished its recombinant expression (Extended Data Fig. 7c,d and Supplementary Fig. 1d). Moreover, another two mutations on cysteine residues, C3313F and C3340Y (corresponding to C3306 and C3333 in mouse, respectively), would disrupt zinc ion coordination within the ZZ domain of dystrophin. As a result, they may induce misfolding and instability of

the ZZ domain, ultimately leading to diminished interactions between dystrophin and the transmembrane DAPs. Consistently, these mutations have been reported to cause reduced or absent subsarcolemmal expression of dystrophin in patients with DMD, further supporting our analysis (Extended Data Table 3).

Discussion

In this study, we present the cryo-EM structure of the native DGC isolated from mouse skeletal muscle. Our findings not only provide an important framework for understanding many previous biochemical studies, but also offer new insights into the assembly of the complex. Specifically, the previous model of the DGC suggested that the sarcoglycan and sarcospan form an independent subcomplex that has a relatively minor role in complex assembly compared with the central position of α -DG and β -DG^{6,7} (Extended Data Fig. 1a). By contrast, our model highlights the central role of sarcoglycans in this process (Extended Data Fig. 8). The large ECD tower, formed by β -, γ - and δ -sarcoglycans, provides a substantial platform on which the extracellular domains of α -DG and α -sarcoglycan can dock. Of note, our model reveals that sarcospan and sarcoglycans do not interact directly with each other. Instead, they are positioned adjacent to both sides of β -DG, thereby stabilizing its single transmembrane helix. The structure also reveals the involvement of a phosphatidylserine-like phospholipid in the interface between the ZZ domain of dystrophin and the transmembrane helices of the sarcoglycans, implying a crucial role for lipids in mediating DGC assembly.

Our cryo-EM structure reveals a distinct conformation of the WW domain of dystrophin, which has been reported to directly interact with the C terminus of β -DG in a previous crystal structure³⁴ (Extended Data Fig. 6d). Consequently, the C terminus of β -DG is absent in the cryo-EM structure, probably owing to potential steric clash with the conformationally altered WW domain of dystrophin (Extended Data Fig. 6d). Previous studies have demonstrated that phosphorylation modifications on both the C terminus of β -DG and the CR domain of dystrophin regulate their interaction. Specifically, phosphorylation of Ser3059 on the WW domain of dystrophin enhances this association, whereas phosphorylation of two tyrosine residues on the C terminus of β -DG disrupts the interaction^{42,43}. Additionally, Thr3074 on the WW domain of dystrophin has been identified as a phosphorylation site that may also regulate the interface interaction, given its proximity to the binding site of the C terminus of β -DG⁴² (Extended Data Fig. 6d). These findings suggest that the interaction interface between dystrophin and the C terminus of β -DG can vary under different physiological conditions, such as changes in phosphorylation status, and that the cryo-EM and crystal structures may represent two different conformational states of the WW domain. The binding of the C terminus of β -DG to dystrophin is expected to induce a local conformational change in the WW domain, potentially affecting the association of nearby dystrobrevin and other associated signalling proteins such as syntrophins. Consequently, this mechanism could contribute to the regulation of signalling pathways mediated by the DGC.

The structure of the DGC offers valuable insights into its function in linking the ECM with the intracellular cytoskeleton, thereby facilitating cellular mechanotransduction. The DGC is oriented perpendicular to the cell membrane, and features a prominent extension of approximately 250 Å, which is significantly longer than its dimensions in the other two directions (Fig. 1). This elongated structure provides a molecular basis for efficient communication between the two sides of the cell membrane. The interplay among the DGC components, particularly the co-folding assembly of β -, γ - and δ -sarcoglycans, forms a rigid and stable core for complex assembly. The extensive interactions between the cytosolic dystrophin and the transmembrane DAPs further establish a longitudinal axis connecting the ECM and intracellular cytoskeleton. Consequently, force exerted on one

side of the DGC can be effectively transmitted to the opposing side through this axis.

The ECD tower of the DGC is reminiscent of the VgrG spike found in the baseplate of bacterial type VI secretion system (T6SS) and the tail spike of bacteriophages (Extended Data Fig. 4c). These spikes also possess a β -helical structure that is used to perforate target membranes. The similarity between the ECD tower and these spikes suggests ECD may have a role in maintaining close proximity to the ECM, facilitating the interaction between α -DG and the ECM. A recent study found that the β -helical domain of a bacteriophage can undergo conformational changes upon binding to the receptor⁴⁴ (Extended Data Fig. 4c). It is possible that the ECD tower of the DGC utilizes a similar mechanism to facilitate mechanical transduction. The characteristic tilt angle of the ECD tower implies that it may also have a role in force transmission by fine-tuning this angle. The tilting of the ECD tower also enables transmission of forces in both longitudinal and lateral directions, thereby contributing to the function of the DGC.

Notably, whereas the core of the DGC is rigid, the two distal ends of the complex are connected by flexible regions and are invisible in our cryo-EM structure. On the extracellular side, the mucin-like domain of α -DG and its interacting LG4 and LG5 domains of laminin- α 2 are unobserved, primarily owing to the flexible nature of the mucin-like domain. On the intracellular side, the N-terminal actin-binding domain and subsequent spectrin domains of dystrophin are also invisible. Sequence and predicted structure analysis of dystrophin suggest the presence of few flexible linkers among these unresolved domains (Extended Data Fig. 6a). We speculate that these structural features may serve as a molecular spring or a buffer for mechanotransduction, ensuring that minor force disturbances are absorbed and not transmitted through the DGC. Only when the cell undergoes substantial changes that exceed a force threshold, such as muscle fibre contraction, would these be transmitted through the DGC across the cell membrane. Therefore, the structural characteristics of the DGC not only ensure effective transmission of mechanical forces between the intracellular and extracellular environments, but may also prevent the conduction of inconsequential mechanical force.

The function of the DGC parallels that of the integrin complex, as both are involved in connecting the ECM and cytoskeleton. Integrins are heterodimeric receptors that are widespread in many cell types and facilitate a diverse array of cell–ECM interactions, having important roles in cell adhesion, cytoskeletal integrity and bidirectional signalling across the plasma membrane⁴⁵. Unlike the DGC, the structures of integrins have been more extensively characterized. Previous structural studies of integrins have revealed marked conformational changes of the ectodomain in ligand-binding sites that are linked to changes in the association of the transmembrane domains between the α - and β -subunits⁴⁶. Notably, integrins exhibit functional complementarity with the DGC to some extent. Mutations in integrin genes have been implicated in causing muscular dystrophies^{47,48}. Interestingly, the upregulation of integrin α 7 β 1 subunit has been observed in patients with DMD and in *mdx* mice, which lack dystrophin⁴⁹. The upregulation of integrin may partially compensate for the loss of functional DGC. Additionally, sarcospan has been reported to genetically interact with integrins, mediating the functional crosstalk between the DGC and integrins⁵⁰. Despite certain functional complementarity, our study highlights substantial differences in the molecular composition and assembly of the DGC and integrin complexes. These findings establish an important structural foundation for enhancing our understanding of the distinct and specific roles of each complex in maintaining cell membrane stability and providing mechanical support in different cellular contexts.

Online content

Any methods, additional references, Nature Portfolio reporting summaries, source data, extended data, supplementary information,

acknowledgements, peer review information; details of author contributions and competing interests; and statements of data and code availability are available at <https://doi.org/10.1038/s41586-024-08310-2>.

- Campbell, K. P. & Kahl, S. D. Association of dystrophin and an integral membrane glycoprotein. *Nature* **338**, 259–262 (1989).
- Ibraghimov-Beskrovnyaya, O. et al. Primary structure of dystrophin-associated glycoproteins linking dystrophin to the extracellular matrix. *Nature* **355**, 696–702 (1992).
- Ervasti, J. M. & Campbell, K. P. A role for the dystrophin-glycoprotein complex as a transmembrane linker between laminin and actin. *J. Cell Biol.* **122**, 809–823 (1993).
- McNally, E. M. & Pytel, P. Muscle diseases: the muscular dystrophies. *Annu. Rev. Pathol.* **2**, 87–109 (2007).
- Duan, D. S., Goemans, N., Takeda, S., Mercuri, E. & Aartsma-Rus, A. Duchenne muscular dystrophy. *Nat. Rev. Dis. Primers* **7**, 13 (2021).
- Durbbeej, M. & Campbell, K. P. Muscular dystrophies involving the dystrophin-glycoprotein complex: an overview of current mouse models. *Curr. Opin. Genet. Dev.* **12**, 349–361 (2002).
- Wilson, D. G. S., Tinker, A. & Iskratsch, T. The role of the dystrophin glycoprotein complex in muscle cell mechanotransduction. *Commun. Biol.* **5**, 1022 (2022).
- Gao, Q. Q. & McNally, E. M. The dystrophin complex: structure, function, and implications for therapy. *Compr. Physiol.* **5**, 1223–1239 (2015).
- Gumerson, J. D. & Michele, D. E. The dystrophin-glycoprotein complex in the prevention of muscle damage. *J. Biomed. Biotechnol.* **2011**, 210797 (2011).
- Lapidos, K. A., Kakkar, R. & McNally, E. M. The dystrophin glycoprotein complex: signaling strength and integrity for the sarcolemma. *Circ. Res.* **94**, 1023–1031 (2004).
- Belhasan, D. C. & Akaaboune, M. The role of the dystrophin glycoprotein complex on the neuromuscular system. *Neurosci. Lett.* **722**, 134833 (2020).
- Pilgram, G. S. K., Potikanond, S., Baines, R. A., Fradkin, L. G. & Noordermeer, J. N. The roles of the dystrophin-associated glycoprotein complex at the synapse. *Mol. Neurobiol.* **41**, 1–21 (2010).
- Constantin, B. Dystrophin complex functions as a scaffold for signalling proteins. *Bochim. Biophys. Acta* **1838**, 635–642 (2014).
- Hoffman, E. P., Brown, R. H. & Kunkel, L. M. Dystrophin—the protein product of the Duchenne muscular dystrophy locus. *Cell* **51**, 919–928 (1987).
- Koenig, M., Monaco, A. P. & Kunkel, L. M. The complete sequence of dystrophin predicts a rod-shaped cytoskeletal protein. *Cell* **53**, 219–228 (1988).
- Rybakova, I. N., Patel, J. R. & Ervasti, J. M. The dystrophin complex forms a mechanically strong link between the sarcolemma and costameric actin. *J. Cell Biol.* **150**, 1209–1214 (2000).
- Bhat, H. F. et al. ABC of multifaceted dystrophin glycoprotein complex (DGC). *J. Cell. Physiol.* **233**, 5142–5159 (2018).
- Deyst, K. A., Bowe, M. A., Leszyk, J. D. & Fallon, J. R. The α -dystroglycan- β -dystroglycan complex. Membrane organization and relationship to an agrin receptor. *J. Biol. Chem.* **270**, 25956–25959 (1995).
- Holt, K. H., Crosbie, R. H., Venzke, D. P. & Campbell, K. P. Biosynthesis of dystroglycan: processing of a precursor propeptide. *FEBS Lett.* **468**, 79–83 (2000).
- Martin, P. T. Dystroglycan glycosylation and its role in matrix binding in skeletal muscle. *Glycobiology* **13**, 55R–66R (2003).
- Sciandra, F. et al. Identification of the β -dystroglycan binding epitope within the C-terminal region of α -dystroglycan. *Eur. J. Biochem.* **268**, 4590–4597 (2001).
- Crosbie, R. H., Heighway, J., Venzke, D. P., Lee, J. C. & Campbell, K. P. Sarcospan, the 25-kDa transmembrane component of the dystrophin-glycoprotein complex. *J. Biol. Chem.* **272**, 31221–31224 (1997).
- Wein, N., Alfano, L. & Flanigan, K. M. Genetics and emerging treatments for Duchenne and Becker muscular dystrophy. *Pediatr. Clin. North. Am.* **62**, 723–742 (2015).
- Mah, J. K. et al. A systematic review and meta-analysis on the epidemiology of Duchenne and Becker muscular dystrophy. *Neuromuscular Disord* **24**, 482–491 (2014).
- Nigro, V. & Savarese, M. Genetic basis of limb-girdle muscular dystrophies: the 2014 update. *Acta Myol* **33**, 1–12 (2014).
- Brown, S. C. et al. Abnormalities in alpha-dystroglycan expression in MDC1C and LGMD2I muscular dystrophies. *Am. J. Pathol.* **164**, 727–737 (2004).
- Michele, D. E. et al. Post-translational disruption of dystroglycan-ligand interactions in congenital muscular dystrophies. *Nature* **418**, 417–422 (2002).
- Barresi, R. & Campbell, K. P. Dystroglycan: from biosynthesis to pathogenesis of human disease. *J. Cell Sci.* **119**, 199–207 (2006).
- Waite, A., Brown, S. C. & Blake, D. J. The dystrophin-glycoprotein complex in brain development and disease. *Trends Neurosci.* **35**, 487–496 (2012).
- Tsubata, S. et al. Mutations in the human δ -sarcoglycan gene in familial and sporadic dilated cardiomyopathy. *J. Clin. Invest.* **106**, 655–662 (2000).
- Guiraud, S. et al. The pathogenesis and therapy of muscular dystrophies. *Annu. Rev. Genomics Hum. Genet.* **16**, 281–308 (2015).
- Norwood, F. L. M., Sutherland-Smith, A. J., Keep, N. H. & Kendrick-Jones, J. The structure of the N-terminal actin-binding domain of human dystrophin and how mutations in this domain may cause Duchenne or Becker muscular dystrophy. *Structure* **8**, 481–491 (2000).
- Muthu, M., Richardson, K. A. & Sutherland-Smith, A. J. The crystal structures of dystrophin and utrophin spectrin repeats: implications for domain boundaries. *PLoS ONE* **7**, e40066 (2012).
- Huang, X. et al. Structure of a WW domain containing fragment of dystrophin in complex with β -dystroglycan. *Nat. Struct. Biol.* **7**, 634–638 (2000).
- Bozic, D., Sciandra, F., Lamba, D. & Brancaccio, A. The structure of the N-terminal region of murine skeletal muscle α -dystroglycan discloses a modular architecture. *J. Biol. Chem.* **279**, 44812–44816 (2004).
- Briggs, D. C. et al. Structural basis of laminin binding to the LARGE glycans on dystroglycan. *Nat. Chem. Biol.* **12**, 810–814 (2016).
- Ramaswamy, K. S. et al. Lateral transmission of force is impaired in skeletal muscles of dystrophic mice and very old rats. *J. Physiol.* **589**, 1195–1208 (2011).
- Singh, J. et al. Proteolytic enzymes and altered glycosylation modulate dystroglycan function in carcinoma cells. *Cancer Res.* **64**, 6152–6159 (2004).
- Jung, D., Yang, B., Meyer, J., Chamberlain, J. S. & Campbell, K. P. Identification and characterization of the dystrophin anchoring site on beta-dystroglycan. *J. Biol. Chem.* **270**, 27305–27310 (1995).
- Chan, Y. M. & Kunkel, L. M. In vitro expressed dystrophin fragments do not associate with each other. *FEBS Lett.* **410**, 153–159 (1997).
- SadoulletPuccio, H. M., Rajala, M. & Kunkel, L. M. Dystrobrevin and dystrophin: An interaction through coiled-coil motifs. *Proc. Natl Acad. Sci. USA* **94**, 12413–12418 (1997).
- Swiderski, K. et al. Phosphorylation within the cysteine-rich region of dystrophin enhances its association with β -dystroglycan and identifies a potential novel therapeutic target for skeletal muscle wasting. *Hum. Mol. Genet.* **23**, 6697–6711 (2014).
- Illesley, J. L., Sudol, M. & Winder, S. J. The interaction of dystrophin with β -dystroglycan is regulated by tyrosine phosphorylation. *Cell Signal* **13**, 625–632 (2001).
- Ge, X. & Wang, J. W. Structural mechanism of bacteriophage lambda tail's interaction with the bacterial receptor. *Nat. Commun.* **15**, 4185 (2024).
- Hynes, R. O. Integrins: bidirectional, allosteric signaling machines. *Cell* **110**, 673–687 (2002).
- Luo, B. H., Carman, C. V. & Springer, T. A. Structural basis of integrin regulation and signaling. *Annu. Rev. Immunol.* **25**, 619–647 (2007).
- Guo, C. et al. Absence of $\alpha 7$ integrin in dystrophin-deficient mice causes a myopathy similar to Duchenne muscular dystrophy. *Hum. Mol. Genet.* **15**, 989–998 (2006).
- Rooney, J. E. et al. Severe muscular dystrophy in mice that lack dystrophin and $\alpha 7$ integrin. *J. Cell Sci.* **119**, 2185–2195 (2006).
- Hodges, B. L. et al. Altered expression of the $\alpha 7 \beta 1$ integrin in human and murine muscular dystrophies. *J. Cell Sci.* **110**, 2873–2881 (1997).
- Marshall, J. L. & Crosbie-Watson, R. H. Sarcospan: a small protein with large potential for Duchenne muscular dystrophy. *Skelet. Muscle* **3**, 1 (2013).

Publisher's note Springer Nature remains neutral with regard to jurisdictional claims in published maps and institutional affiliations.

Springer Nature or its licensor (e.g. a society or other partner) holds exclusive rights to this article under a publishing agreement with the author(s) or other rightsholder(s); author self-archiving of the accepted manuscript version of this article is solely governed by the terms of such publishing agreement and applicable law.

© The Author(s), under exclusive licence to Springer Nature Limited 2024

Methods

Animals

Wild-type C57BL/6J mice, aged 2–4 months old, were used for DGC sample preparation. Mice were maintained in barrier facilities with a strictly controlled macroenvironment, including a temperature of 20–26 °C, humidity ranges of 40–70%, and a 12-h light/12-h dark cycle. All animal studies and experiments were conducted in compliance with institutional guidelines and approved by the Institutional Animal Care and Use Committee (IACUC) at Westlake University, Hangzhou, China.

Expression and purification of the LG4 and LG5 domains of laminin- α 2

DNA encoding residues 2730–3118 of the mouse LG4 and LG5 domains of laminin- α 2 (UniProt ID: Q60675) was amplified from a cDNA library derived from mouse skeletal muscle and inserted into the pCAG vector downstream of a CMV promoter. The native signal peptide preceding laminin- α 2 LG4–LG5 was included. Additionally, a 3×Flag tag was fused to the carboxyl terminus of laminin- α 2 LG4–LG5. The constructed plasmid was transfected into HEK293F cells (Thermo Fisher Scientific) using polyethylenimine (PEI) when the cell density reached 2×10^6 cells per ml. The transfected cells were cultured in SMM 293-TII Expression medium (Sino Biological) at 37 °C under 5% CO₂. After 4 days of expression, the cell culture media was collected and diluted 1.6-fold with double-distilled water. The diluted media was loaded onto Source 15S beads (GE Healthcare) on an AKTA Purifier (GE Healthcare). The beads were extensively washed with buffer A (25 mM MOPS-Na, pH 7.4, 2 mM CaCl₂), and the bound protein was eluted using a buffer with a linear gradient of salt concentration. The protein eluted at approximately 130 mM NaCl was further purified using size-exclusion chromatography (Superose 6 Increase, 10/300 GL, GE Healthcare) in a buffer containing 25 mM MOPS-Na, pH 7.4, 150 mM NaCl, 2 mM CaCl₂. The fractions corresponding to the peak were pooled, flash-frozen in liquid nitrogen, and stored at –80 °C until use.

Membrane isolation from mouse skeletal muscle

We followed a previously reported method with slight modifications⁵¹. All steps were conducted at 4 °C. About 100 g skeletal muscle from mouse legs were homogenized in a buffer containing 25 mM MOPS-Na, pH 7.4, 0.3 M sucrose, and 2 mM phenylmethylsulfonyl fluoride (PMSF). Following homogenization, the sample was centrifuged at 6,000g for 6 min. The supernatant was carefully collected and stored on ice. The pellet was subjected to homogenization and centrifugation twice more. All supernatant was pooled and spun at 200,000g for 1 h to pellet the membrane. The membrane was then washed twice by resuspending in a buffer containing 25 mM MOPS-Na, pH 7.4, 600 mM KCl, 165 mM sucrose, and 2 mM PMSF, followed by centrifugation at 200,000g for 1 h. The pellet was flash-frozen in liquid nitrogen and stored at –80 °C until use.

Endogenous purification of the DGC

The membrane prepared from mouse skeletal muscle was solubilized at 4 °C for 2 h in a buffer containing 25 mM MOPS-Na, pH 7.4, 300 mM NaCl, 2 mM CaCl₂, 1% glyco-diosgenin (GDN), 3.9 μ g ml^{–1} aprotinin, 2.1 μ g ml^{–1} pepstatin, 15 μ g ml^{–1} leupeptin, 2 mM PMSF, and 1.5 mg of Flag-tagged LG4–LG5 domains of laminin- α 2. The insoluble fraction was pelleted by centrifugation at 20,000g for 1 h, and the supernatant was then incubated with anti-Flag G1 affinity resin (GenScript) at 4 °C for 1 h. The resin was washed with a buffer containing 25 mM MOPS-Na, pH 7.4, 300 mM NaCl, 2 mM CaCl₂, 0.01% GDN, and 1 mM PMSF for 100-fold the volume of the resin. The target protein complex was eluted with a buffer containing 25 mM MOPS-Na, pH 7.4, 250 mM NaCl, 2 mM CaCl₂, 0.01% GDN and 250 μ g ml^{–1} Flag peptide. The eluted protein was concentrated and applied to size-exclusion chromatography (Superose 6 Increase, 10/300 GL, GE Healthcare) equilibrated in a buffer composed

of 25 mM MOPS-Na, pH 7.4, 150 mM NaCl, 2 mM CaCl₂, 0.01% GDN. The fractions containing the DGC were pooled and concentrated for further experiments.

Expression and purification of the extracellular domains of α -sarcoglycan and dystroglycan

DNA encoding residues 1–250 of mouse α -sarcoglycan (UniProt ID: P82350) or residues 1–27 (signal peptide) and 492–712 of mouse dystroglycan (UniProt ID: Q62165) was individually amplified from a cDNA library derived from mouse skeletal muscle. The DNA was then inserted into the pCAG vector, with a 2×Flag tag or a GST tag fused to the carboxyl terminus of α -sarcoglycan and dystroglycan, respectively. The expression of the two domains in HEK293F cells followed a similar protocol as the expression of the LG4–LG5 domains of laminin- α 2 described above. For each expression batch, 0.3 mg plasmids were transfected into 200 ml cells at a density of 2×10^6 cells per ml. After 4 days of expression, the supernatant was collected and loaded onto the anti-Flag G1 affinity resin (GenScript) for α -sarcoglycan or Glutathione Sepharose 4B (GS4B, GE Healthcare) for dystroglycan. After extensive washing with a buffer of 25 mM MOPS-Na, pH 7.4, 300 mM NaCl, α -sarcoglycan was eluted with a buffer containing 25 mM MOPS-Na, pH 7.4, 300 mM NaCl, and 250 μ g ml^{–1} Flag peptide, while dystroglycan was eluted with a buffer containing 25 mM MOPS-Na, pH 7.4, 300 mM NaCl, and 13 mM reduced glutathione. The eluted proteins were then concentrated and subjected to size-exclusion chromatography (Superose 6 Increase, 10/300 GL, GE Healthcare) equilibrated in a buffer composed of 25 mM MOPS-Na, pH 7.4, 150 mM NaCl. All buffers used for purifying dystroglycan contained 2 mM CaCl₂. Fractions obtained from gel filtration were subsequently analysed by SDS–PAGE.

The reported muscular dystrophy-related mutation sites that are observable in the structure have been summarized in Extended Data Table 3^{30,52–75}. Plasmids for 19 disease-related mutations of α -sarcoglycan and the C667F mutation of dystroglycan were generated separately using standard site-directed mutagenesis techniques and verified by DNA sequencing. The expression and purification of these mutants followed the same procedure as their corresponding wild types.

Western blotting

The DGC fractions obtained from size-exclusion chromatography were loaded onto 14% SDS–PAGE gels for electrophoresis. Proteins were then transferred to poly-vinylidene fluoride membrane (Merck Millipore). After blocking with 5% non-fat milk in Tris-buffered saline with Tween 20 (TBST) for 1 h at room temperature, the membrane was incubated with the primary antibodies against dystroglycan, α -, β -, δ - and γ -sarcoglycans, and dystrobrevin. Following primary antibody incubation at room temperature for 1–2 h, the membrane was washed with TBST and then incubated with the HRP-conjugated Goat anti-Rabbit IgG polyclonal antibody (1:50,000 dilution, HUABIO) for 1 h at room temperature. The bands were visualized by eECL Western Blot Kit (CWBI0).

Gel filtration binding assay

The gene encoding mouse dystrophin (3049–3299) or dystrobrevin (1–237) was cloned into a pET21 vector carrying either a C-terminal GST tag or an N-terminal 6×His tag, respectively. BL21(DE3)-CodonPlus-RIPL was individually transformed with the prepared expression plasmids. Induction of protein expression was carried out during the log phase of growth with 0.2 mM isopropyl β -D-1-thiogalactopyranoside for 12 h at 20 °C. The cell pellet was collected and sonicated in lysis buffer containing 25 mM Tris-HCl, pH 8.0, 300 mM NaCl, and 2 mM PMSF. After centrifugation at 20,000g for 1 h to remove the pellet, the supernatant was loaded onto either Glutathione Sepharose 4B (GS4B, GE Healthcare) for GST-tagged dystrophin or TALON Metal Affinity resin (Takara) for 6×His-tagged dystrobrevin. After extensive washing with a buffer containing 25 mM Tris-HCl, pH 8.0, 300 mM NaCl, dystrophin

was eluted with a buffer containing 100 mM Tris-HCl, pH 8.0, 300 mM NaCl, 13 mM reduced glutathione, while dystrobrevin was eluted with a buffer containing 25 mM Tris-HCl, pH 8.0, 300 mM NaCl, 250 mM imidazole. The eluent was concentrated and subjected to size-exclusion chromatography using a Superose 6 Increase column (10/300 GL, GE Healthcare) in buffer containing 25 mM Tris-HCl, pH 8.0, 150 mM NaCl. Fractions corresponding to the peak were pooled, flash-frozen in liquid nitrogen, and stored at -80°C until further use.

For the gel filtration binding assay, 3 μM dystrophin and 30 μM dystrobrevin were mixed in 1 ml buffer containing 25 mM Tris-HCl, pH 8.0, 150 mM NaCl. The proteins were incubated on ice for 1 h before being injected into a Superdex 200 Increase column (10/300 GL, GE Healthcare) pre-equilibrated with the same buffer. As a control, the binding of GST with dystrobrevin was also assessed under the same conditions. Additionally, dystrophin, GST, or dystrobrevin alone were individually applied for gel filtration under the same conditions. The fractions from gel filtration were analysed using SDS-PAGE.

Mass spectrometry analysis

The SDS-PAGE gel containing the target protein band was excised and washed twice with 50% acetonitrile. Subsequently, the sample underwent reduction and alkylation before being digested with trypsin in 50 mM ammonium bicarbonate for 14 h at 37°C . The digested sample was then extracted twice with 1% formic acid in a 50% acetonitrile aqueous solution and dried to powder using a vacuum dryer.

For liquid chromatography-mass spectrometry (LC-MS/MS) analysis, the peptides were resuspended in 0.1% formic acid (w/w) and automatically injected using Bruker's nanoElute UHPLC System onto a 25 cm column equipped with an emitter (Aurora series, CSI, 25 $\mu\text{m} \times 75 \mu\text{m}$ internal diameter, 1.6 μm C18, IonOpticks). The bound peptides were eluted over 60 min at a constant flow rate of 300 nl min^{-1} , with mobile phases consisting of buffer A (0.1% formic acid in H_2O) and buffer B (0.1% formic acid in acetonitrile). The elution gradient started from 2% buffer B and increased to 22% over 45 min, followed by a further increase to 35% buffer B between 45 and 50 min. Eluted peptides were sprayed into a TIMS quadrupole time-of-flight instrument (timsTOF Pro 2, Bruker Daltonics) using a nano-electrospray source (CaptiveSpray source, Bruker Daltonics). Samples were measured in DDA-PASEF mode, with the DDA-PASEF windows scheme ranging in dimension m/z from 300 to 1,500 and in dimension $1/K_0$ from 0.75 to 1.3, with a ramp time 166 ms.

Data files from the LC-MS/MS analysis were processed using Proteome Discoverer 2.5 (Thermo Fisher Scientific) to identify proteins. The Sequest HT search engine was employed with default parameters for protein identification, aiming for a false discovery rate of <0.01 at both the protein and peptide levels. The *Mus musculus* proteome (Proteomes ID: UP000000589) obtained from UniProt was used for the search.

Cryo-EM sample preparation and data acquisition

For cryo-EM sample preparation, 3.5 μl of the DGC sample purified from mouse skeletal muscle was loaded onto a glow-discharged grid (Quantifoil, R1.2/1.3, Cu 300 mesh, coated with 2 nm carbon film). The grid was blotted for 3 s with a blot force of 3 after a 60-s waiting period using the Vitrobot (Mark IV, Thermo Fisher Scientific) under the conditions of 100% humidity at 8°C . Subsequently, the grid was plunge-frozen into liquid ethane cooled by liquid nitrogen. The dataset was collected using a 300 kV Titan Krios microscopy equipped with a Gatan K3 Summit detector and a GIF Quantum energy filter with a 20-eV slit width. Micrographs were automatically acquired in super-resolution mode with a magnification of 81,000 \times using EPU software (Thermo Fisher Scientific). Each micrograph was set within a defocus range of $-1.5 \mu\text{m}$ to $-2.0 \mu\text{m}$ and exposed for 2.56 s with 0.08 s per frame, resulting in 32 frames and an approximate total dose of $50 \text{ e}^{-} \text{ \AA}^{-2}$. A total of 40,736 movie stacks were collected.

Image processing

A flowchart of the data processing steps can be found in Extended Data Fig. 2. A total of 40,736 movie stacks were initially subjected to motion correction with twofold binning using MotionCor2⁷⁶. The dose-weighted micrographs, with a pixel size of 1.087 \AA , were then further processed for patch-based contrast transfer function estimation using CryoSPARC v4⁷⁷. The initial round of auto-picking yielded approximately 22.93 million particles, with a box size of 496 pixels. After multiple rounds of 2D classifications, 911,157 particles were selected for subsequent ab initio reconstruction and heterogeneous refinement; 421,743 particles were then selected for non-uniform refinement⁷⁸, resulting in a reconstruction with an overall resolution of 3.4 \AA (Map 0). The overall quality of the extracellular and transmembrane regions of map 0 is good, but the intracellular region remains poor, rendering this region unassignable.

To further improve the overall map quality, we re-processed the data starting with particle picking using templates generated by Map 0. About 38.26 million particles were picked for seed-facilitated 2D classifications. In general, the picked raw particles were evenly distributed into multiple subgroups, each containing around 1 million raw particles. A subset of about 200,000 high-quality particles from previous 2D classifications were chosen as seed particles. Subsequently, the seed particles were combined with the raw particles within each subgroup to facilitate 2D classifications. Following this step, a total of 34.75 million particles (after eliminating duplicated particles) were selected for 16 parallel runs of heterogeneous refinements ($K = 5-10$). A total of 3.34 million particles were selected and combined from all parallel runs, followed with a subsequent ab initio reconstruction ($K = 5$). We selected 1.34 million particles from the best subset for another round of non-uniform refinement, resulting in a reconstruction with an overall resolution of 3.2 \AA (Map 1). This map shows excellent overall quality and was used to guide model building for the extracellular and transmembrane regions. However, the density corresponding to the intracellular region of Map 1 was still very weak.

To improve the map quality of the intracellular region, particles from the aforementioned seed-facilitated 2D classifications were re-selected with more stringent selection criteria. Only particles that exhibited distinguishable features of the intracellular region were retained. This iterative process yielded 4.91 million particles for subsequent non-uniform refinement. Next, $3\times$ parallel runs of 3D classifications ($K = 8, 12$, and 16) were performed using these particles, with a mask focusing on the intracellular region. The best classes, characterized by clear features within the intracellular region, were selected for a subsequent round of 2D classification. Ultimately, 499,658 particles were selected for a final round of non-uniform refinement, yielding a reconstruction with an overall resolution of 3.5 \AA (Map 2). Map 2 exhibited clearer density in the intracellular area compared with Map 1, which was used for the model building of the intracellular region as well as final model refinement and figure presentation.

The overall map resolution was determined using the gold-standard Fourier shell correlation (FSC) 0.143 criterion. All map figures were generated using UCSF Chimera⁷⁹ or ChimeraX⁸⁰.

Model building and refinement

Model building was based on Map 1 and Map 2 generated from the DGC dataset. The predicted structures of individual or subcomplex of DGC components by AlphaFold2⁸¹ were used as initial templates. Additionally, the crystal structure of human dystrophin WW domain-containing fragment (PDB code:1EG3) was used as the initial model for building dystrophin. These structures were manually docked into the density map in UCSF Chimera following manual adjustments in Coot⁸². Bulky residues such as Arg, Trp, Tyr, Lys and Phe served as landmarks due to their clear visibility in the cryo-EM map. For most of the extracellular and transmembrane regions, side-chain features were clearly resolved, and the modelling was validated by the fitness of the side-chain densities and

the protein sequences. Extra densities in the glycosylation modification sites further facilitated the validation of the modelling. The current cryo-EM density only allows for the assignment of up to three sugar moieties on each glycosylation site. The EF domains of dystrophin and dystrobrevin were built mainly based on docking of crystal structure and predicted structure, respectively, due to their limited side-chain features. A total of 2,092 amino acid residues were modelled. Besides, a phosphatidylserine and three cholesterol-like lipids were identified and modelled in the structure. A zinc and a calcium ion were assigned in the ZZ domain of dystrophin and the immunoglobulin-like domain of α -DG, respectively.

Additionally, a small stretch of density corresponding to a short polypeptide of about five amino acids near the ZZ domain of dystrophin remains unassigned. This density could potentially belong to the C terminus of sarcospan or the N terminus of β -sarcoglycan, as they are in close proximity to this density. Certain additional densities near the zinc-binding motif of the ZZ domain of dystrophin were also unresolved due to limited resolution (Extended Data Fig. 6b). The presence of these densities strongly suggests the existence of additional interfaces through the zinc-binding motif of the ZZ domain that facilitate interactions between dystrophin and DAPs. These further underscore the importance of the ZZ domain of dystrophin in DGC assembly and function.

The final model was refined against Map 2 using real-space refinement in Phenix⁸³. During the refinement process, restraints on secondary structure, Ramachandran plots, and rotamers were applied. Iterative correction with Coot was performed between rounds of Phenix refinement. Statistical data of 3D reconstruction and model refinement are provided in Extended Data Table 1.

Reporting summary

Further information on research design is available in the Nature Portfolio Reporting Summary linked to this article.

Data availability

The cryo-EM maps of the mouse DGC have been deposited at the Electron Microscopy Data Bank (<https://www.ebi.ac.uk/pdbe/emdb/>) under the accession codes EMD-39569 and EMD-39568. The corresponding atomic coordinate data has been deposited at the Protein Data Bank (<http://www.rcsb.org>) under the accession code 8YT8. All data analysed during this study are included in this Article and its Supplementary Information. Any other relevant reagents and materials are available from the corresponding author upon request.

Code availability

No code was used for this study.

51. Yan, Z. et al. Structure of the rabbit ryanodine receptor RyR1 at near-atomic resolution. *Nature* **517**, 50–55 (2015).
52. Diniz, G. et al. Sarcolemmal alpha and gamma sarcoglycan protein deficiencies in Turkish siblings with a novel missense mutation in the alpha sarcoglycan gene. *Pediatr. Neurol.* **50**, 640–647 (2014).
53. Duggan, D. J. et al. Mutations in the sarcoglycan genes in patients with myopathy. *New Engl. J. Med.* **336**, 618–624 (1997).
54. Piccolo, F. et al. Primary adhalinopathy—a common-cause of autosomal recessive muscular-dystrophy of variable severity. *Nat. Genet.* **10**, 243–245 (1995).
55. Carrie, A. et al. Mutational diversity and hot spots in the alpha-sarcoglycan gene in autosomal recessive muscular dystrophy (LGMD2D). *J. Med. Genet.* **34**, 470–475 (1997).
56. Saha, M. et al. Impact of PYROXD1 deficiency on cellular respiration and correlations with genetic analyses of limb-girdle muscular dystrophy in Saudi Arabia and Sudan. *Physiol. Genomics* **50**, 929–939 (2018).
57. Kawai, H. et al. Adhalin gene mutations in patients with autosomal recessive childhood onset muscular dystrophy with adhalin deficiency. *J. Clin. Invest.* **96**, 1202–1207 (1995).
58. Duclos, F. et al. β -sarcoglycan: genomic analysis and identification of a novel missense mutation in the LGMD2E Amish isolate. *Neuromusc. Disord.* **8**, 30–38 (1998).
59. dos Santos, M. R., Jorge, P., Ribeiro, E. M., Pires, M. M. & Guimaraes, A. Novel mutation (Y184C) in exon 4 of the beta-sarcoglycan gene identified in a Portuguese patient. Mutations in brief no. 177. *Hum. Mutat.* **12**, 214–215 (1998).

60. Bonnemann, C. G. et al. Genomic screening for beta-sarcoglycan gene mutations: Missense mutations may cause severe limb-girdle muscular dystrophy type 2E (LGMD 2E). *Hum. Mol. Genet.* **5**, 1953–1961 (1996).
61. Bonnemann, C. G. et al. LGMD 2E in Tunisia is caused by a homozygous missense mutation in β -sarcoglycan exon 3. *Neuromusc. Disord.* **8**, 193–197 (1998).
62. Vermeer, S. et al. Novel mutations in three patients with LGMD2C with phenotypic differences. *Pediatr. Neurol.* **30**, 291–294 (2004).
63. Nowak, K. J. et al. Severe γ -sarcoglycanopathy caused by a novel missense mutation and a large deletion. *Neuromusc. Disord.* **10**, 100–107 (2000).
64. Crosbie, R. H. et al. Molecular and genetic characterization of sarcospan:: insights into sarcoglycan–sarcospan interactions. *Hum. Mol. Genet.* **9**, 2019–2027 (2000).
65. Piccolo, F. et al. A founder mutation in the γ -sarcoglycan gene of Gypsies possibly predating their migration out of India. *Hum. Mol. Genet.* **5**, 2019–2022 (1996).
66. Duggan, D. J. et al. Mutations in the δ -sarcoglycan gene are a rare cause of autosomal recessive limb-girdle muscular dystrophy (LGMD2). *Neurogenetics* **1**, 49–58 (1997).
67. Nigro, V. et al. Identification of a novel sarcoglycan gene at 5q33 encoding a sarcolemmal 35 kDa glycoprotein. *Hum. Mol. Genet.* **5**, 1179–1186 (1996).
68. Moreira, E. S. et al. A first missense mutation in the δ sarcoglycan gene associated with a severe phenotype and frequency of limb-girdle muscular dystrophy type 2 F (LGMD2F) in Brazilian sarcoglycanopathies. *J. Med. Genet.* **35**, 951–953 (1998).
69. Geis, T. et al. Homozygous dystroglycan mutation associated with a novel muscle-eye-brain disease-like phenotype with multicystic leucodystrophy. *Neurogenetics* **14**, 205–213 (2013).
70. Dai, Y. et al. Whole exome sequencing identified a novel DAG1 mutation in a patient with rare, mild and late age of onset muscular dystrophy-dystroglycanopathy. *J. Cell. Mol. Med.* **23**, 811–818 (2019).
71. Feng, J., Yan, J., Buzin, C. H., Towbin, J. A. & Sommer, S. S. Mutations in the dystrophin gene are associated with sporadic dilated cardiomyopathy. *Mol. Genet. Metab.* **77**, 119–126 (2002).
72. Flanigan, K. M. et al. Rapid direct sequence analysis of the dystrophin gene. *Am. J. Hum. Genet.* **72**, 931–939 (2003).
73. Vulin, A. et al. The ZZ domain of dystrophin in DMD: making sense of missense mutations. *Hum. Mutat.* **35**, 257–264 (2014).
74. Goldberg, L. R. et al. A dystrophin missense mutation showing persistence of dystrophin and dystrophin-associated proteins yet a severe phenotype. *Ann. Neurol.* **44**, 971–976 (1998).
75. Lenk, U. et al. A cysteine 3340 substitution in the dystroglycan-binding domain of dystrophin associated with Duchenne muscular dystrophy, mental retardation and absence of the ERG b-wave. *Hum. Mol. Genet.* **5**, 973–975 (1996).
76. Zheng, S. Q. et al. MotionCor2: anisotropic correction of beam-induced motion for improved cryo-electron microscopy. *Nat. Methods* **14**, 331–332 (2017).
77. Punjani, A., Rubinstein, J. L., Fleet, D. J. & Brubaker, M. A. cryoSPARC: algorithms for rapid unsupervised cryo-EM structure determination. *Nat. Methods* **14**, 290–296 (2017).
78. Punjani, A., Zhang, H. & Fleet, D. J. Non-uniform refinement: adaptive regularization improves single-particle cryo-EM reconstruction. *Nat. Methods* **17**, 1214–1221 (2020).
79. Pettersen, E. F. et al. UCSF chimera—a visualization system for exploratory research and analysis. *J. Comput. Chem.* **25**, 1605–1612 (2004).
80. Pettersen, E. F. et al. UCSF ChimeraX: structure visualization for researchers, educators, and developers. *Protein Sci.* **30**, 70–82 (2021).
81. Jumper, J. et al. Highly accurate protein structure prediction with AlphaFold. *Nature* **596**, 583–589 (2021).
82. Emsley, P. & Cowtan, K. Coot: model-building tools for molecular graphics. *Acta Crystallogr. D* **60**, 2126–2132 (2004).
83. Afonine, P. V. et al. Real-space refinement in PHENIX for cryo-EM and crystallography. *Acta Crystallogr. D* **74**, 531–544 (2018).

Acknowledgements The authors thank the cryo-EM Facility of Westlake University for providing support on cryo-EM data collection; Westlake University HPC Center for computational resources and related assistance; the Mass Spectrometry and Metabolomics Core Facility of Westlake University for mass spectrometry analysis. This work was supported by National Natural Science Foundation of China (32271261 to J.W. and 32271239 to Z.Y.), Zhejiang Provincial Natural Science Foundation of China (LR22C050003 to J.W.), Westlake University (1011103860222B1 to J.W. and 1011103560222B1 to Z.Y.) and Westlake Education Foundation (101486021901 to J.W. and 101456021901 to Z.Y.). Research reported in this publication was also supported by the National Institute of Neurological Disorders and Stroke of the National Institutes of Health under Award Number P50NS053672 to K.P.C. K.P.C. is an investigator of the Howard Hughes Medical Institute.

Author contributions J.W. and Z.Y. conceived and supervised the project. J.W., Z.Y. and L.W. designed the experiments. L.W. prepared the protein samples, collected cryo-EM datasets and performed all other biochemical experiments. X.G., Q.X. and G.H. performed the cryo-EM data processing. Q.X. and J.W. built the atomic model. T.Y. and K.P.C. advised on DGC protein preparation and contributed to manuscript discussions. All authors contributed to data analysis. J.W., Z.Y. and L.W. wrote the manuscript with input from all co-authors.

Competing interests The authors declare no competing interests.

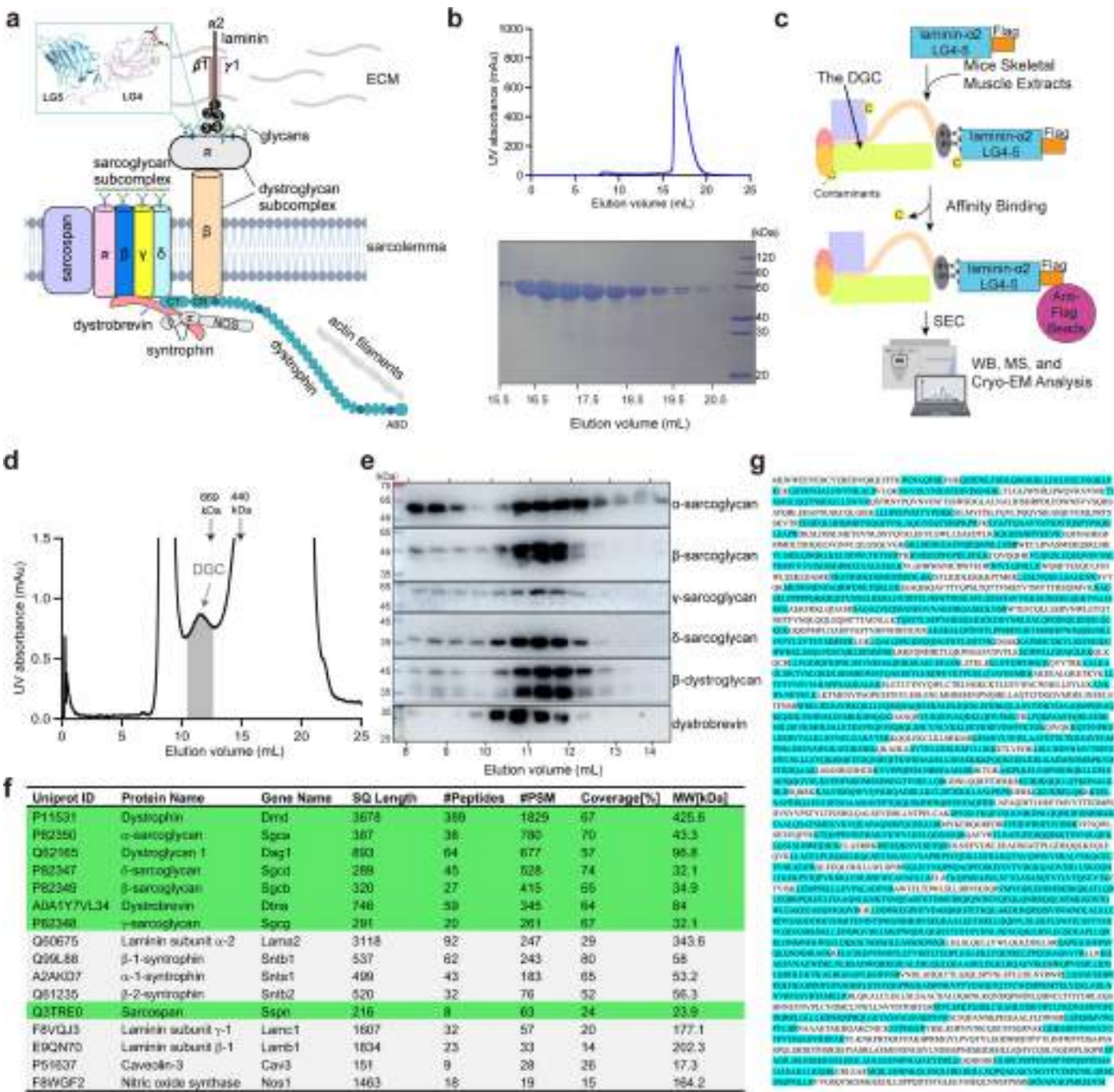
Additional information

Supplementary information The online version contains supplementary material available at <https://doi.org/10.1038/s41586-024-08310-2>.

Correspondence and requests for materials should be addressed to Zhen Yan or Jianping Wu.

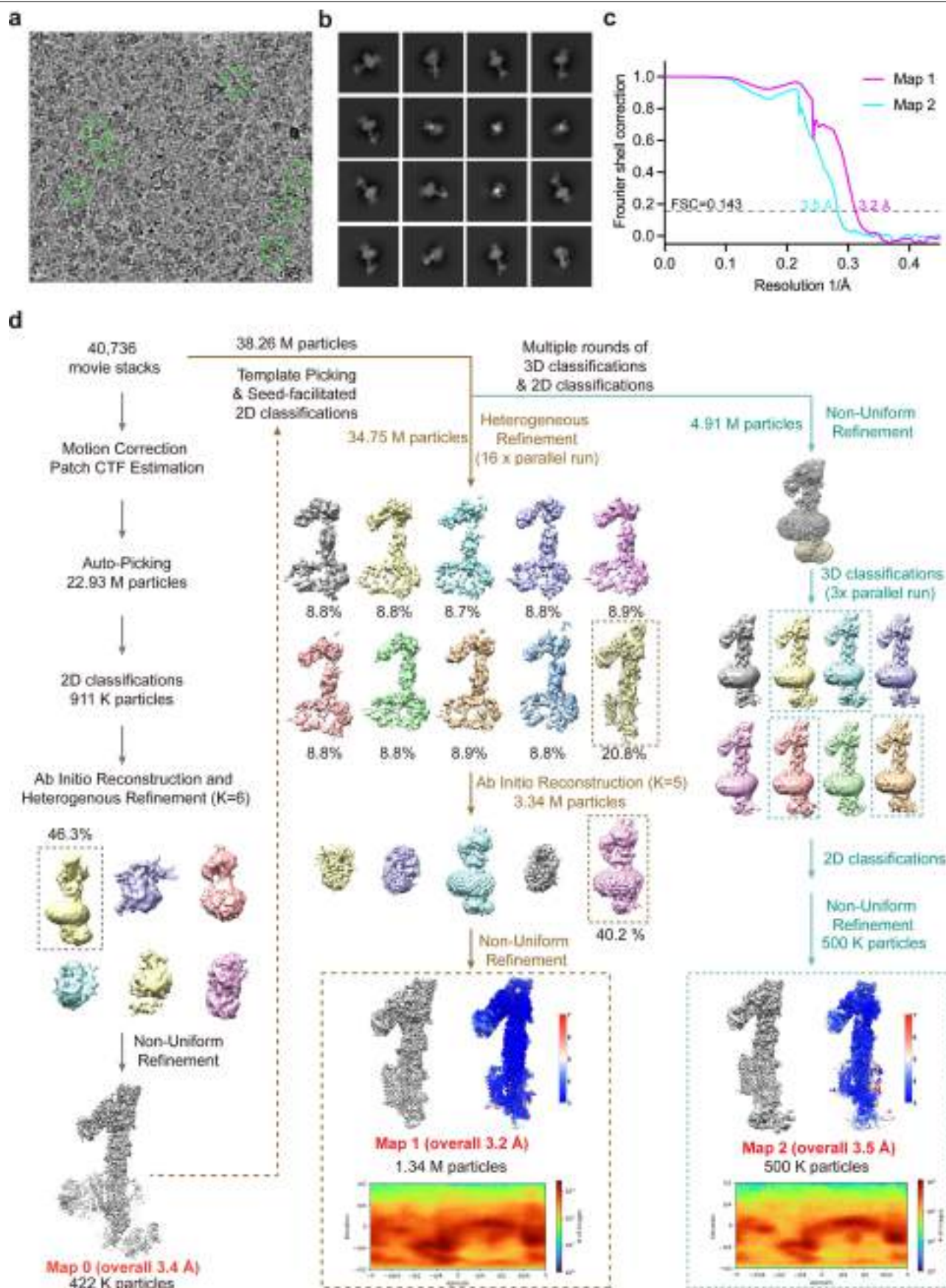
Peer review information Nature thanks Jeffrey Chamberlain and the other, anonymous, reviewer(s) for their contribution to the peer review of this work. Peer review reports are available.

Reprints and permissions information is available at <http://www.nature.com/reprints>.



Extended Data Fig. 1 | Endogenous purification of the DGC from mouse skeletal muscle. a, A classic schematic showing the overall organization of the DGC. The LG4 and LG5 domains of laminin-α2 interact with the glycans on α-DG. Inset: crystal structure of the LG4 and LG5 domains of laminin-α2 in complex with glycans (PDB: 5IK5). ECM: extracellular matrix; ABD: actin-binding domain; CR: cysteine-rich domain; CT: C-terminal domain. **b**, Size exclusion chromatogram and corresponding SDS-PAGE analysis of the purified LG4 and LG5 domains of laminin-α2. Purifications were repeated independently at least three times with similar results. **c**, A diagram showing the purification procedure of the native DGC from mouse skeletal muscle. SEC: size exclusion chromatography; WB: western blot; MS: mass spectrometry. **d**, Size exclusion

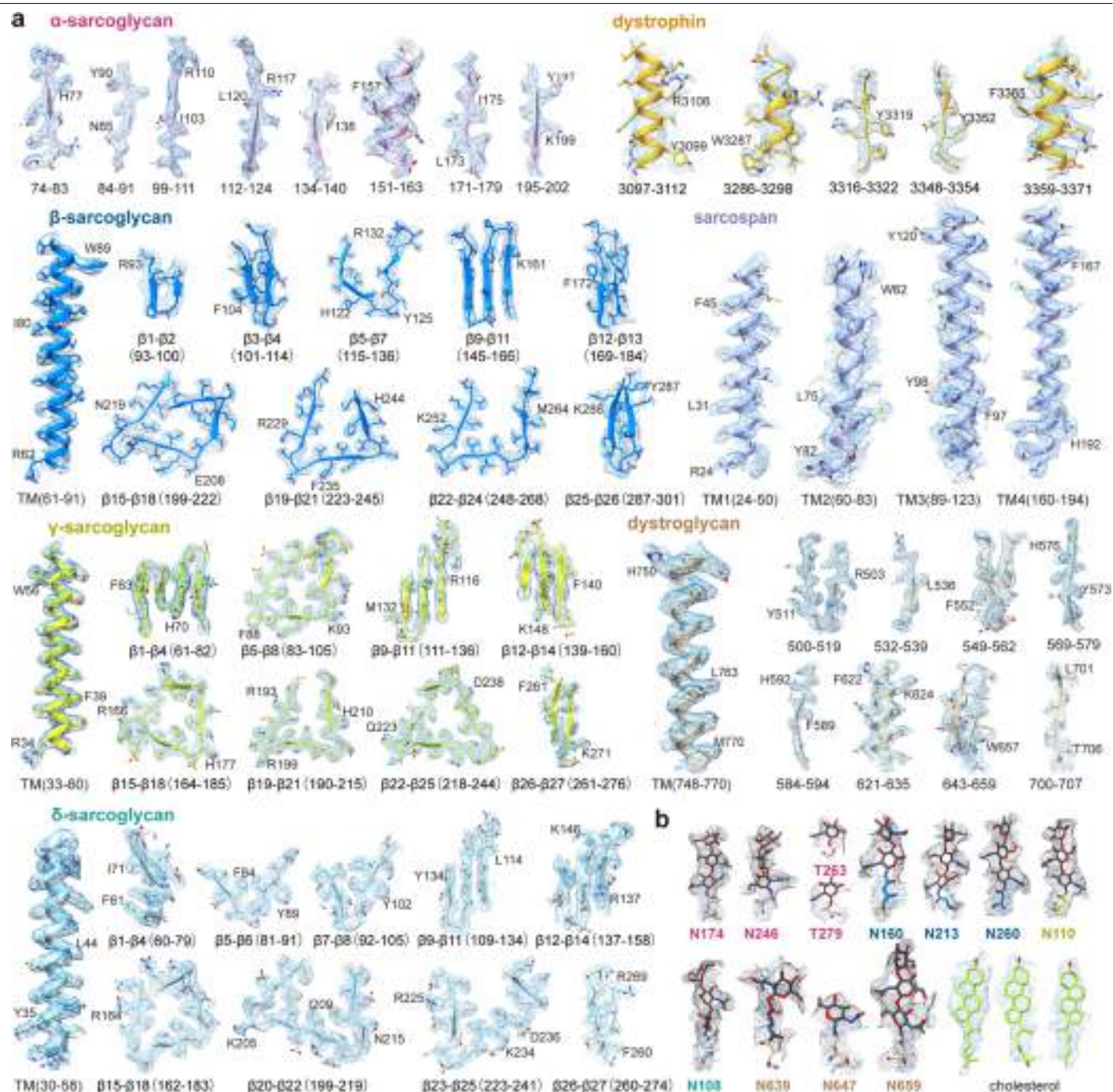
chromatography profile of the purified DGC sample. The shaded fractions were collected for cryo-EM and MS analysis. **e**, Western blot analysis of the gel filtration fractions against multiple DGC components. Each western blot was repeated at least twice with similar results. For gel source data, see Supplementary Fig. 1a. **f**, MS analysis of the purified DGC sample. Potential DGC components are listed in the order of decreasing peptide-spectrum match (PSM) scores. The DGC components observed in our model are highlighted in green. **g**, Peptide identification of dystrophin by MS analysis of the purified DGC sample. The identified regions are shaded in cyan, which account for a total of 67% sequence coverage.



Extended Data Fig. 2 | See next page for caption.

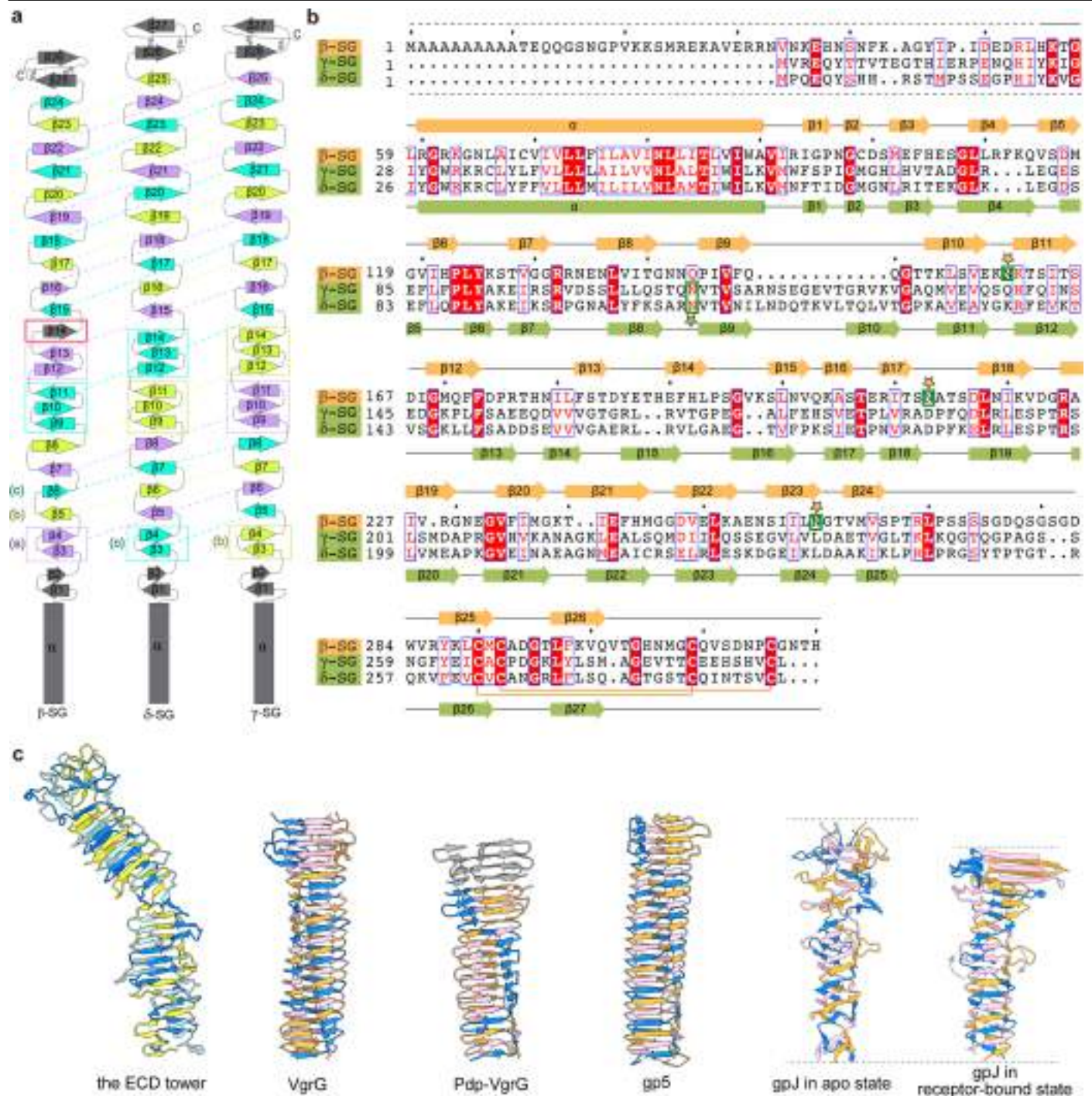
Extended Data Fig. 2 | Cryo-EM data analysis of the DGC. **a**, A raw cryo-EM image of the purified DGC sample out of a dataset of 40,736 images. Representative particles are highlighted by green circles. Scale bar: 50 nm. **b**, Two-dimensional class averages. Box size: 469.6 Å. **c**, Gold-standard Fourier shell correlation (FSC) curves of the final maps. **d**, A flowchart of cryo-EM data processing.

For details, see 'Image processing' in the Methods. Map 1 (EMDB-39569) is the map with the highest overall resolution and Map 2 (EMDB-39568) is the map with the clearest intracellular densities. Both maps were used to guide model building. The local resolutions of the two maps were estimated by cryoSPARC.



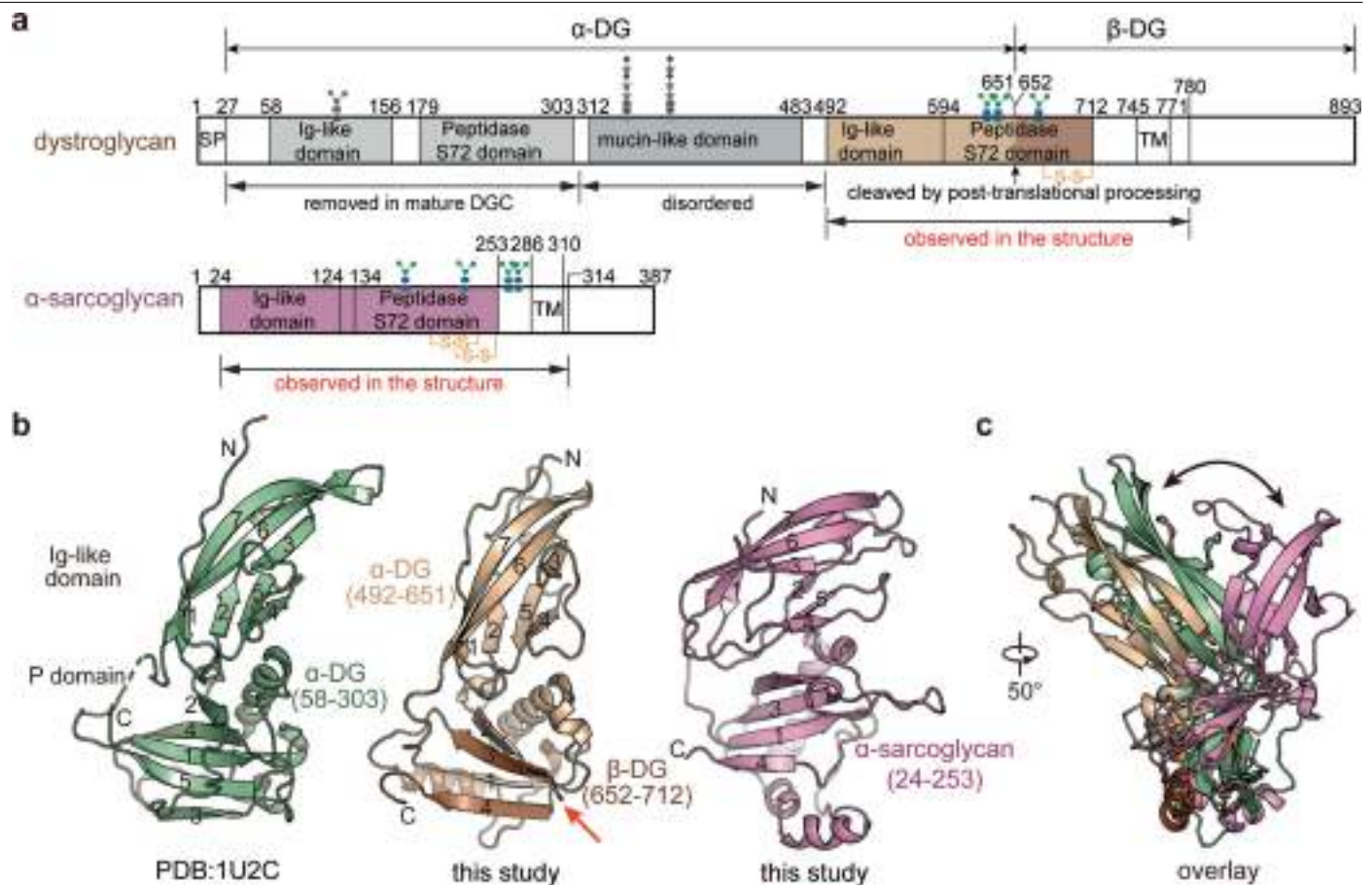
Extended Data Fig. 3 | Density maps of the DGC components. **a**, Density maps of selected segments of each DGC component. The density of dystrobrevin is presented in Fig. 4f. The boundaries of each segment and some bulky residues

are labelled. **b**, The glycan densities of all identified glycosylation sites and the densities of three cholesterol-like lipids. The density maps were generated in ChimeraX.



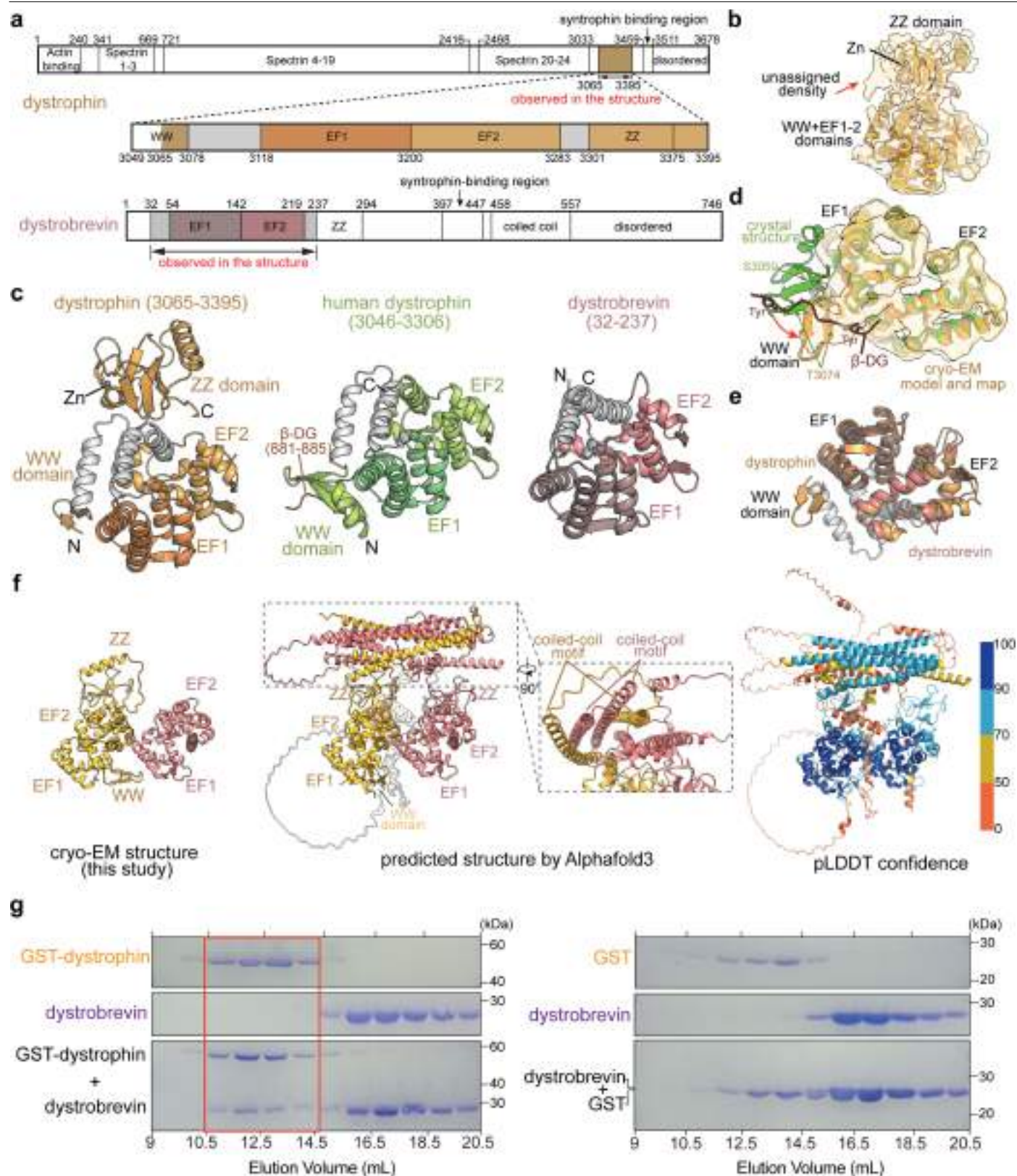
Extended Data Fig. 4 | Structural topology and sequence alignment of β -, γ -, and δ -sarcoglycans. **a**, Topological diagram of β -, γ -, and δ -sarcoglycans. The β strands on face (a), (b), and (c) of the ECD tower are coloured in purple, green, and cyan, respectively. The anti-parallel β strands within the same face of the ECD tower are boxed. The β 14 strand of β -sarcoglycan, which differs from the other two sarcoglycans, is highlighted by a red box. The β strands on each face of the ECD tower are connected by coloured dashed lines. **b**, Sequence alignment among β -, γ -, and δ -sarcoglycans. Secondary structure elements of β -sarcoglycan are labelled above the sequence and that of γ - and δ -sarcoglycans are indicated by dashed lines. Glycosylation sites are indicated by green boxes and asterisks. Disulfide bonds are labelled by orange lines. The UniProt IDs for each sequence are as follows: β -sarcoglycan: P82349, γ -sarcoglycan: P82348, δ -sarcoglycan: P82347. **c**, Structural comparison among several β -helical-containing proteins. The structures presented include the β -helical domains of the ECD tower of the DGC, VgrG (PDB: 6SK0), Pdp-VgrG (PDB: 6U9E), gp5 from the T4 bacteriophage (PDB: 1K28), and gpJ in closed/apo (PDB: 8XCK) and open/receptor-bound (PDB: 8XCJ) states. The relative rotational and overall height changes of gpJ between the apo and receptor-bound states are indicated by grey arrows and dashed lines, respectively.

are indicated by dashed lines. Glycosylation sites are indicated by green boxes and asterisks. Disulfide bonds are labelled by orange lines. The UniProt IDs for each sequence are as follows: β -sarcoglycan: P82349, γ -sarcoglycan: P82348, δ -sarcoglycan: P82347. **c**, Structural comparison among several β -helical-containing proteins. The structures presented include the β -helical domains of the ECD tower of the DGC, VgrG (PDB: 6SK0), Pdp-VgrG (PDB: 6U9E), gp5 from the T4 bacteriophage (PDB: 1K28), and gpJ in closed/apo (PDB: 8XCK) and open/receptor-bound (PDB: 8XCJ) states. The relative rotational and overall height changes of gpJ between the apo and receptor-bound states are indicated by grey arrows and dashed lines, respectively.



Extended Data Fig. 5 | Domain organization of dystroglycan and α -sarcoglycan. **a**, Schematic diagrams of dystroglycan and α -sarcoglycan. The resolved extracellular domains of the two components are shaded in colour. Glycosylation sites and disulfide bonds are labelled. SP: signal peptide. **b**, Structural comparisons among the extracellular domains of dystroglycan and α -sarcoglycan. The red arrow indicates the reported dividing point

between α -DG and β -DG, situated in the loop region between the $\beta 2$ and $\beta 3$ strands of the P domain. **c**, Structural overlay among the extracellular domains of dystroglycan and α -sarcoglycan. The three models are superimposed by their P domains. The double-headed arrow indicates conformational variations of the immunoglobulin-like domains.

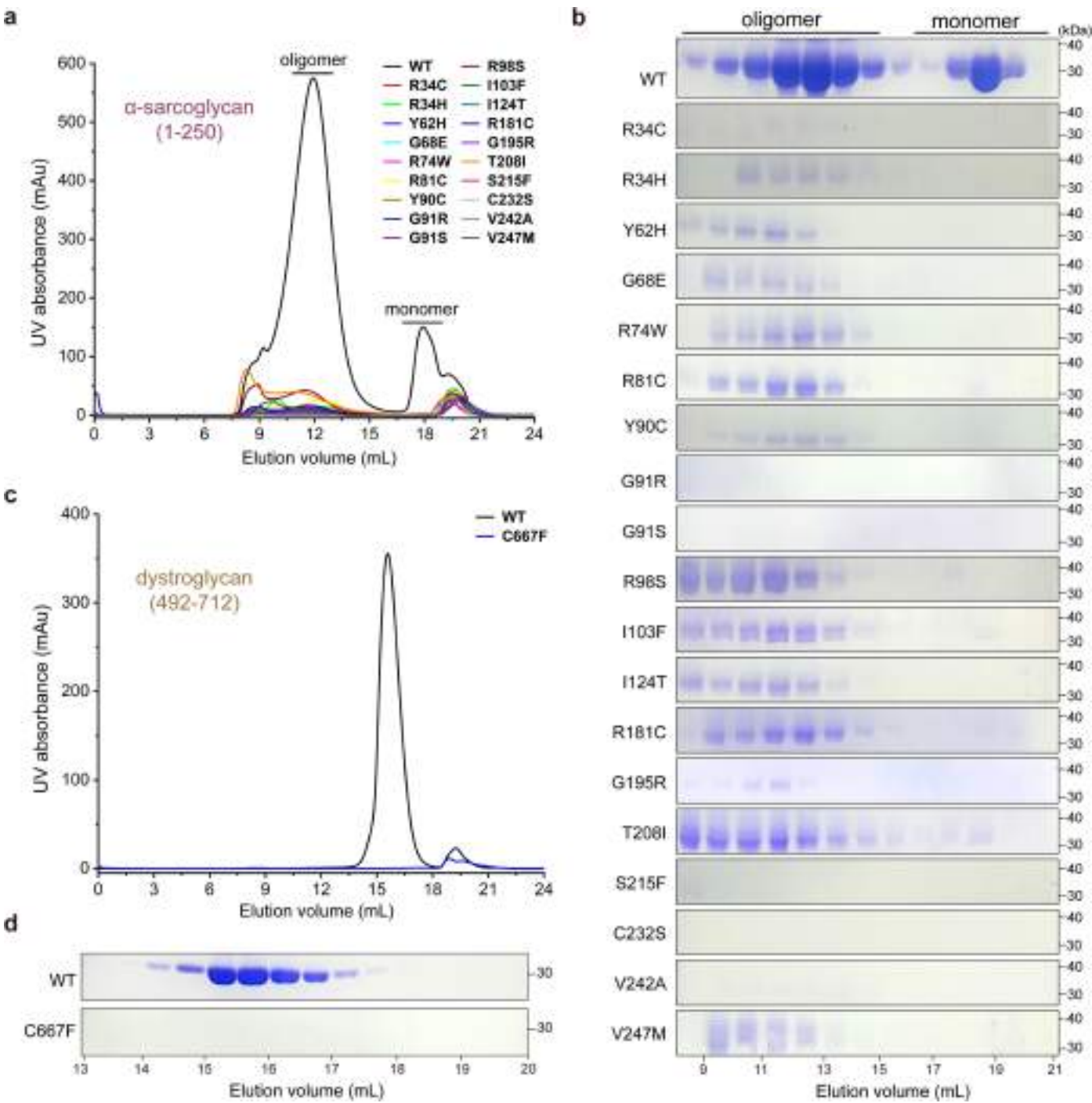


Extended Data Fig. 6 | See next page for caption.

Extended Data Fig. 6 | Interaction between dystrophin and dystrobrevin.

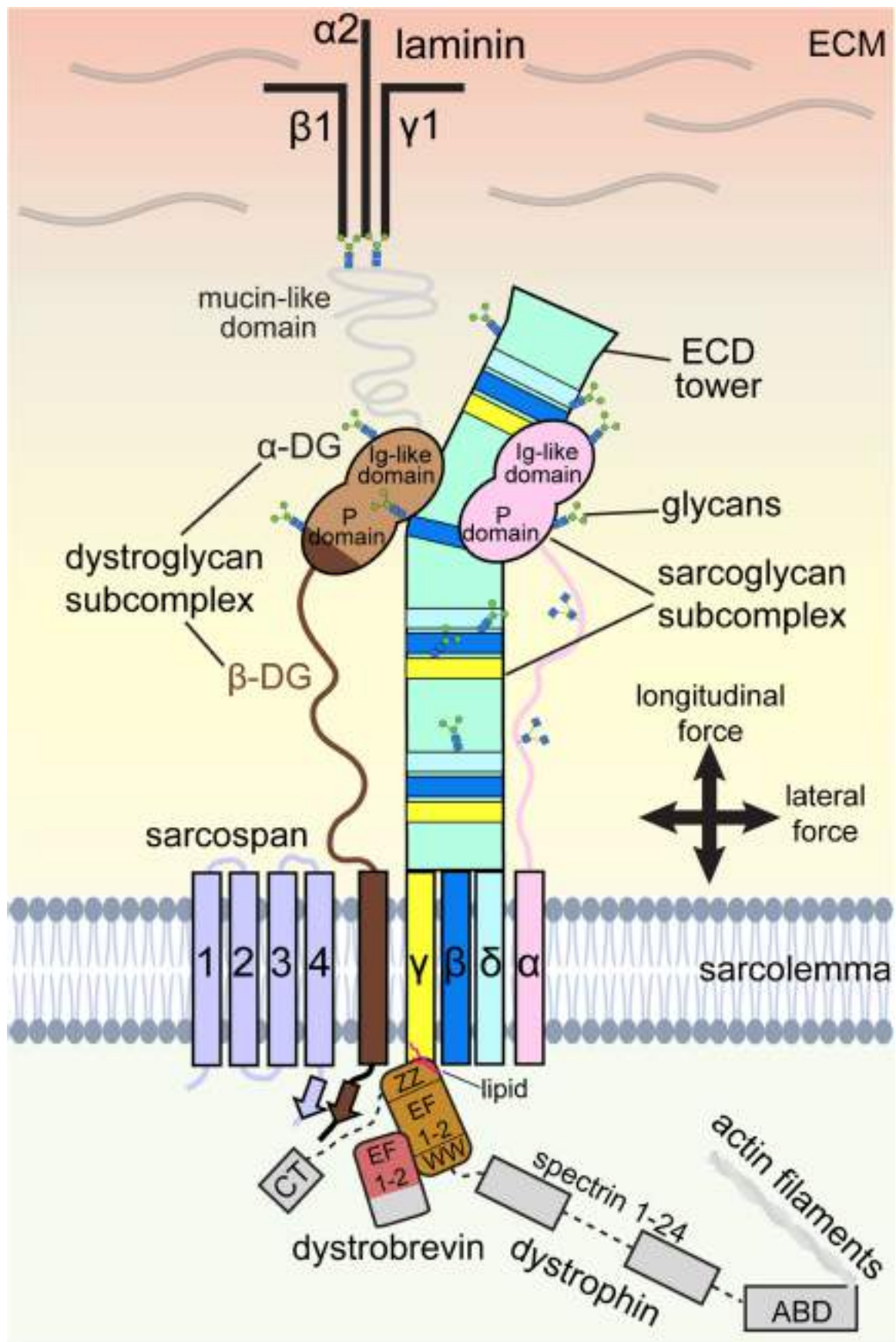
a, Schematic diagram of dystrophin and dystrobrevin. **b**, Structure of CR domain of dystrophin fitted onto the cryo-EM map. The map is shown as a transparent surface. The red arrow indicates extra unassigned density near the zinc-binding site of the ZZ domain. **c**, Overall structure of the resolved domains of dystrophin and dystrobrevin. The crystal structure of human dystrophin in complex with the C-terminus of β -DG peptide (PDB:1EG4) is also presented for comparison. The domains are coloured in the same scheme as in **a**. **d**, Comparison of the crystal structure and the cryo-EM structure of the WW and EF-hand domains of dystrophin. The cryo-EM density map of this region is shown as a transparent surface. The red arrow indicates the conformational deviation of the WW domain between the two structures. S3059 and T3074 on the WW domain of

dystrophin, and two tyrosine residues on the C-terminus of β -DG, which have been reported as phosphorylation sites, are shown as sticks. **e**, Structural overlay of the EF-hand domains in dystrobrevin and dystrophin. **f**, Comparison between the cryo-EM structure and the predicted structure by AlphaFold3. The predicted structure between dystrophin (3049–3678) and dystrobrevin (1–746) suggests the presence of two major interaction interfaces. **g**, Gel filtration binding assay to verify the interaction between dystrobrevin and dystrophin. Left: dystrobrevin co-migrates with the GST-tagged dystrophin. Right: dystrobrevin does not co-migrate with GST alone. The co-migration of dystrobrevin and GST-tagged dystrophin is highlighted by a red box. The assay was repeated independently three times with similar results. For gel source data, see Supplementary Fig. 1b.



Extended Data Fig. 7 | Recombinant expression of the extracellular domains of α -sarcoglycan and dystroglycan. a, Size-exclusion chromatogram of wild-type and 19 disease-related mutations of α -sarcoglycan (1–250). In addition to the monomeric peak, the recombinantly expressed protein also exhibits an oligomeric peak, possibly due to heterologous overexpression in HEK293 cells.

b, SDS-PAGE analysis of the purified wild-type and disease-related mutations of α -sarcoglycan. For gel source data, see Supplementary Fig. 1c. **c**, Size-exclusion chromatogram of wild-type and the C667F mutation of dystroglycan (492–712). **d**, SDS-PAGE analysis of the purified wild-type and the C667F mutation of dystroglycan. For gel source data, see Supplementary Fig. 1d.



Extended Data Fig. 8 | See next page for caption.

Article

Extended Data Fig. 8 | A modified schematic of the DGC based on our structure. In this model, sarcoglycans play a central role in complex assembly. In the extracellular side, β -, γ -, and δ -sarcoglycans co-fold to form a large ECD tower, which serves as docking sites for multiple extracellular domains from other components. In the transmembrane region, the sarcoglycans and sarcospan flank two sides of the transmembrane of β -DG, thereby stabilizing

the latter. In the cytoplasmic region, sarcoglycans and β -DG directly interact with the ZZ domain of dystrophin. The structural features of the DGC, including the characteristic tilt angle of the ECD tower, enable it to efficiently connect the two sides of sarcolemma and transmit both longitudinal and lateral forces.

DGC complex (EMD-39569, EMD-39568) (PDB 8YT8)			
Data collection and processing			
Microscope	PEI Titan Krios		
Magnification	81,000		
Detector	Gatan K3		
Electron exposure (e ⁻ /Å ²)	50		
Defocus range (μm)	-1.4 ~ -1.9		
Pixel size (Å)	1.087		
Symmetry imposed	C1		
Maps	Map 1	Map 2	
Final particle images (No.)	1,340,346	499,658	
Map resolution (Å)	3.2	3.5	
FSC threshold	0.143		
Map resolution range (Å)	3.0 ~ 7.5	3.2 ~ 6.2	
EMDB code	EMD-39569	EMD-39568	
Refinement			
Initial model used (PDB code)	None		
Map sharpening B factor (Å ²)	-60.5	-94.7	
Model composition			
Non-hydrogen atoms	16,309		
Protein residues	2,092		
Lipids	4		
Ion	2		
R.m.s. deviations			
Bond length (Å)	0.004		
Bond angles (°)	1.019		
Validation			
Molprobity score	1.91		
Clashscore	9.61		
Poor rotamers (%)	0.24		
Ramachandran plot			
Favored (%)	93.92		
Allowed (%)	5.93		
Disallowed (%)	0.14		

Article

Extended Data Table 2 | Summary of model building of the DGC

Subunit /Chain ID in model	Length (aa) /Uniprot ID	Modelled Regions /Coverage	Domains	Modifications	
				Glycosylations	Disulfide bonds
α-sarcoglycan /A	387 /P82350	23-314 /75.4%	Ig-like: 24-124; P: 134-253; TM: 286-314	N174, N246, T263, T279	C209-C232 C222-C245
β-sarcoglycan /B	320 /P82349	47-317 /84.7%	TM: 62-92; ECD tower: 93-317	N160, N213, N260	C290-C309 C292-C316
γ-sarcoglycan /G	291 /P82348	24-291 /92.1%	TM: 31-60; ECD tower: 61-291;	N110	C265-C283 C267-C290
δ-sarcoglycan /D	289 /P82347	28-289 /90.7%	TM: 29-59; ECD tower: 60-289;	N108	C263-C281 C288-C265
sarcospan /S	216 /Q62147	24-200 /88.5%	TM1: 25-50; TM2: 55-83; TM3: 89-124; TM4: 157-189	-	C128-C137 C135-C157
dystrobrevin /C	746 /Q9D2N4	32-237 /86.5%	EF1: 54-142; EF2:143-219	-	-
dystrophin /E	3678 /P11531	3065-3392 /8.9%	WW: 3065-3078; EF1: 3118-3200; EF2: 3201-3283; ZZ: 3301-3375	-	-
dystroglycan /O	893 /Q62165	492-780 /32.4%	Ig-like: 492-594; P: 595-712; TM: 745-771	N639, N647, N659	C667-C711

Extended Data Table 3 | Disease-related mutants on the DGC

Protein Name	Mutations in human	Residues in mouse	Phenotype	Ref
α-sarcoglycan	Q25*	Q25	LGMD2D	52
	L31P	L31	LGMD2D	53
	R34C/H	R34	LGMD2D	53,55
	Y62H	Y62	LGMD2D	54
	G68E	G68	LGMD2D	54
	R74W	R74	LGMD2D	56
	L76F	L76	LGMD2D	56
	Q80*	Q80	LGMD2D	54
	R81C	R81	LGMD2D	56
	L89F/P	L89	LGMD2D	52
	Y90C	Y90	LGMD2D	52
	G91S/R	G91	LGMD2D	52,54,55
	D97G	D97	DMD-like	53
	R98H/S/C	R98	LGMD2D	52,53
	Q101*	Q101	LGMD2D	52
	I103F/T	I103	LGMD2D	52,53,55
	R110L	R110	LGMD2D	52
	I124T	I124	LGMD2D	53,55
	Y134*	Y134	LGMD2D	52
	E137K/R/G	E137	LGMD2D	52,53,57
	L139R	L139	LGMD2D	52
	R141S	R141	LGMD2D	52
	F157S	F157	LGMD2D	52
	L158F	L158	LGMD2D	53,55
	L173P	L173	LGMD2D	53
	R181C	R181	LGMD2D	52
	R192*	R192	LGMD2D	52
	G195R	G195	LGMD2D	52
	V196I	V196	LGMD2D	53
	P205S/H	P205	LGMD2D	52,53
	T208A	T208	LGMD2D	52
	T208I	T208	LGMD2D	52
	S215F	S215	LGMD2D	52
	R221H	R221	LGMD2D	52
	C222Y	C222	LGMD2D	52
Protein Name	Mutations in human	Residues in mouse	Phenotype	Ref
α-sarcoglycan	P228Q	P228	DMD-like	53
	C232S/W	C232	LGMD2D	52
	V242A/F	V242	LGMD2D	52,54
	V247M	V247	LGMD2D	54
	R284C	R284	LGMD2D	53,54
β-sarcoglycan	M312R	M312	LGMD2D	52
	R91C/L/P	R93	LGMD2E	58-61
	M100K	M102	LGMD2E	60
	L108R	L110	LGMD2E	60
	S114F	S116	DMD-like	53,55
γ-sarcoglycan	G139*	G141	DMD	53
	T151R	T153	LGMD2E	60
	T182A	T184	DMD	53,55
	Y184C/ Y184*	Y186	LGMD2E	53,59
	W31*	W31	LGMD2C	62
δ-sarcoglycan	G69R	G69	LGMD2C	63
	Δ525T#	Δ525T	LGMD2C	64
	L194S	L194	LGMD2C	52,63
	C283Y	C283	LGMD2C	63,65
	W29*	W29	DMD	66
dystroglycan	S150A	S150	LGMD2F	30
	R164*	R164	DMD	66
	N210Y	N210	LGMD2F	67
	E261K	E261	LGMD2F	68
	C669F	C667	CMD	69
dystrophin	R776C	R774	LGMD2P†	70
	F3228L	F3221	CMD3B	71
	C3313F	C3306	DMD	72,73
	D3335H	D3328	DMD	73,74
	C3340Y	C3333	DMD	73,75

The mutations reported to cause severe, intermediate, and mild phenotypes are shaded in red, blue, and green, respectively. Other mutations do not have a clear severity reported. *: premature translation termination; #: the Δ525T mutation results in a frameshift at codon 175, leading to the production of 18 additional missense amino acids until a premature termination at codon 194; †: also known as Muscular Dystrophy-Dystroglycanopathy, Type C, 9 (MDDGC9); LGMD: Limb-girdle muscular dystrophy; CMD3B: Cardiomyopathy, dilated, X-linked 3B; DMD: Duchenne-like muscular dystrophy.

Reporting Summary

Nature Portfolio wishes to improve the reproducibility of the work that we publish. This form provides structure for consistency and transparency in reporting. For further information on Nature Portfolio policies, see our [Editorial Policies](#) and the [Editorial Policy Checklist](#).

Statistics

For all statistical analyses, confirm that the following items are present in the figure legend, table legend, main text, or Methods section.

n/a Confirmed

- | | | |
|-------------------------------------|-------------------------------------|--|
| <input type="checkbox"/> | <input checked="" type="checkbox"/> | The exact sample size (n) for each experimental group/condition, given as a discrete number and unit of measurement |
| <input checked="" type="checkbox"/> | <input type="checkbox"/> | A statement on whether measurements were taken from distinct samples or whether the same sample was measured repeatedly |
| <input checked="" type="checkbox"/> | <input type="checkbox"/> | The statistical test(s) used AND whether they are one- or two-sided
<i>Only common tests should be described solely by name; describe more complex techniques in the Methods section.</i> |
| <input checked="" type="checkbox"/> | <input type="checkbox"/> | A description of all covariates tested |
| <input checked="" type="checkbox"/> | <input type="checkbox"/> | A description of any assumptions or corrections, such as tests of normality and adjustment for multiple comparisons |
| <input checked="" type="checkbox"/> | <input type="checkbox"/> | A full description of the statistical parameters including central tendency (e.g. means) or other basic estimates (e.g. regression coefficient) AND variation (e.g. standard deviation) or associated estimates of uncertainty (e.g. confidence intervals) |
| <input checked="" type="checkbox"/> | <input type="checkbox"/> | For null hypothesis testing, the test statistic (e.g. F , t , r) with confidence intervals, effect sizes, degrees of freedom and P value noted
<i>Give P values as exact values whenever suitable.</i> |
| <input checked="" type="checkbox"/> | <input type="checkbox"/> | For Bayesian analysis, information on the choice of priors and Markov chain Monte Carlo settings |
| <input checked="" type="checkbox"/> | <input type="checkbox"/> | For hierarchical and complex designs, identification of the appropriate level for tests and full reporting of outcomes |
| <input checked="" type="checkbox"/> | <input type="checkbox"/> | Estimates of effect sizes (e.g. Cohen's d , Pearson's r), indicating how they were calculated |

Our web collection on [statistics for biologists](#) contains articles on many of the points above.

Software and code

Policy information about [availability of computer code](#)

Data collection EPU2.12.0

Data analysis MotionCor2, CryoSPARC 4.4.1, UCSF Chimera 1.17.3, UCSF ChimeraX 1.6.1, Coot 0.9.8.8, AlphaFold2, AlphaFold3, PHENIX 1.19.2, PyMOL 2.5.0, Proteome Discoverer 2.5.

For manuscripts utilizing custom algorithms or software that are central to the research but not yet described in published literature, software must be made available to editors and reviewers. We strongly encourage code deposition in a community repository (e.g. GitHub). See the Nature Portfolio [guidelines for submitting code & software](#) for further information.

Data

Policy information about [availability of data](#)

All manuscripts must include a [data availability statement](#). This statement should provide the following information, where applicable:

- Accession codes, unique identifiers, or web links for publicly available datasets
- A description of any restrictions on data availability
- For clinical datasets or third party data, please ensure that the statement adheres to our [policy](#)

The cryo-EM maps of the mouse DGC have been deposited at the Electron Microscopy Data Bank (<https://www.ebi.ac.uk/pdbe/emdb/>) under the accession codes EMD-39569 and EMD-39568. The corresponding atomic coordinate data has been deposited at the Protein Data Bank (<http://www.rcsb.org>) under the accession

code 8YT8. All data analyzed during this study are included in this Article and its Supplementary Information. Any other relevant reagents are available from the corresponding author upon reasonable request.

Research involving human participants, their data, or biological material

Policy information about studies with [human participants or human data](#). See also policy information about [sex, gender \(identity/presentation\), and sexual orientation](#) and [race, ethnicity and racism](#).

Reporting on sex and gender N/A

Reporting on race, ethnicity, or other socially relevant groupings N/A

Population characteristics N/A

Recruitment N/A

Ethics oversight N/A

Note that full information on the approval of the study protocol must also be provided in the manuscript.

Field-specific reporting

Please select the one below that is the best fit for your research. If you are not sure, read the appropriate sections before making your selection.

☒ Life sciences ☐ Behavioural & social sciences ☐ Ecological, evolutionary & environmental sciences

For a reference copy of the document with all sections, see [nature.com/documents/nr-reporting-summary-flat.pdf](https://www.nature.com/documents/nr-reporting-summary-flat.pdf)

Life sciences study design

All studies must disclose on these points even when the disclosure is negative.

Sample size	Sample size for the cryo-EM dataset was determined by the availability of the microscope time and the particle density on the grids. Sufficient cryo-EM micrographs were collected to achieve the reported high-resolution EM maps, which is sufficient for model building. The sample size was also confirmed by size exclusion chromatography and western blot.
Data exclusions	For cryo-EM analysis, micrographs with bad CTF fitting were discarded. Only high-resolution and homogeneous particles were kept to generate the final high-resolution maps.
Replication	All attempts for the results replication such as the protein purifications and the binding assays were successful according to the protocol described in the Methods section. The numbers of replication were described in the figure legends.
Randomization	CryoEM extracted particles were assigned to several independent groups with each 2D classification was assigned randomly with the random orientation. During 3D refinement process, the particles were randomly divided into separate groups.
Blinding	For all experiments including the binding assay and the mutants' effects on the expression in this study, there was positive or negative control and all results were obtained in parallel under the same experimental conditions.

Reporting for specific materials, systems and methods

We require information from authors about some types of materials, experimental systems and methods used in many studies. Here, indicate whether each material, system or method listed is relevant to your study. If you are not sure if a list item applies to your research, read the appropriate section before selecting a response.

Materials & experimental systems

n/a	Involved in the study
<input type="checkbox"/>	<input checked="" type="checkbox"/> Antibodies
<input type="checkbox"/>	<input checked="" type="checkbox"/> Eukaryotic cell lines
<input checked="" type="checkbox"/>	<input type="checkbox"/> Palaeontology and archaeology
<input type="checkbox"/>	<input checked="" type="checkbox"/> Animals and other organisms
<input checked="" type="checkbox"/>	<input type="checkbox"/> Clinical data
<input checked="" type="checkbox"/>	<input type="checkbox"/> Dual use research of concern
<input checked="" type="checkbox"/>	<input type="checkbox"/> Plants

Methods

n/a	Involved in the study
<input checked="" type="checkbox"/>	<input type="checkbox"/> ChIP-seq
<input checked="" type="checkbox"/>	<input type="checkbox"/> Flow cytometry
<input checked="" type="checkbox"/>	<input type="checkbox"/> MRI-based neuroimaging

Antibodies

Antibodies used	Primary antibodies: unconjugated DAG1 Rabbit pAb (Abclonal, Cat# A10076, RRID:AB_2757599), unconjugated beta-sarcoglycan (SGCB) Rabbit pAb (Abclonal, Cat# A6979, RRID:AB_2767535), unconjugated alpha-sarcoglycan (SGCA) Rabbit mAb (Abclonal, Cat# A19754, RRID: AB_3097789, clone name: ARC2280), unconjugated delta-sarcoglycan (SGCD) Rabbit mAb (Abclonal, Cat# A9175, RRID:AB_2863679, clone name: ARC1463), unconjugated dystrobrevin (DTNA) Rabbit pAb (Proteintech, Cat# 10741-1-AP, RRID: AB_2093895), unconjugated gamma sarcoglycan (SGCG) rabbit monoclonal antibody (Abmart, Cat# TU344124, RRID:AB_3097790). Secondary antibody: HRP-Conjugated Goat anti-Rabbit IgG Goat Polyclonal antibody (HUABIO, Cat# HA1001, RRID:AB_2819166)
Validation	The primary antibody against DAG1 was validated using the various cell lines such as HepG2, U2OS, SW480, HeLa, as well as the extracts from mouse skeletal muscle, mouse lung, mouse heart and rat liver. The primary antibody against SGCB was validated using the extracts from SKOV3 cell line, mouse heart, mouse skeletal muscle, and rat heart. The primary antibody against SGCA was validated using the extracts from rat heart and rat skeletal muscle. The primary antibody against SGCD was validated using the extracts from mouse heart. The primary antibody against DTNA was validated using the lysates from mouse heart and rat heart. The primary antibody against SGCG was validated using the lysates of mouse muscle tissue. All primary antibodies were shown to detect corresponding target.

Eukaryotic cell lines

Policy information about [cell lines and Sex and Gender in Research](#)

Cell line source(s)	HEK293F cell line was purchased from Thermo Fisher Scientific Inc. (Cat#R79007, RRID: CVCL_D603)
Authentication	No further authentication was performed for commercially available HEK293F cell line since the protein used in this study was expressed successfully with HEK293 cells.
Mycoplasma contamination	The cell line was not tested for mycoplasma contamination.
Commonly misidentified lines (See ICLAC register)	There is no commonly misidentified cell lines used in this study.

Animals and other research organisms

Policy information about [studies involving animals; ARRIVE guidelines](#) recommended for reporting animal research, and [Sex and Gender in Research](#)

Laboratory animals	Species: mouse, strain: C57BL/6J, age: 2-4 months. Mice were maintained in barrier facilities with a strictly controlled macroenvironment, including a temperature of 20-26°C, humidity ranges of 40-70%, and a 12-hour light/12-hour dark cycle.
Wild animals	The study did not involve wild animals.
Reporting on sex	The mice sex was not considered in this study.
Field-collected samples	No field-collected samples were used in this study.
Ethics oversight	All animal maintenance and experimental procedures used in this study were conducted in compliance with institutional guidelines and approved by the Institutional Animal Care and Use Committee (IACUC) at Westlake University, Hangzhou, China.

Note that full information on the approval of the study protocol must also be provided in the manuscript.

Plants

Seed stocks	N/A
Novel plant genotypes	N/A
Authentication	N/A